

Natural Hyperbolicity of Hexagonal Boron Nitride in the Deep Ultraviolet

Bongjun Choi¹, Jason Lynch¹, Wangleong Chen², Seong-Joon Jeon³, Hyungseob Cho³, Kyungmin Yang¹, Jonghwan Kim^{3,4,5*}, Nader Engheta^{1,2,6,7*}, Deep Jariwala^{1,2*}

¹Department of Electrical and Systems Engineering, University of Pennsylvania, Philadelphia, Pennsylvania 19104, United States

²Department of Materials Science and Engineering, University of Pennsylvania, Philadelphia, Pennsylvania 19104, United States

³Department of Materials Science and Engineering, Pohang University of Science and Technology, Pohang, Republic of Korea.

⁴Department of Physics, Pohang University of Science and Technology, Pohang, Republic of Korea.

⁵Center for van der Waals Quantum Solids, Institute for Basic Science (IBS), Pohang, Republic of Korea

⁶Department of Bioengineering, University of Pennsylvania, Philadelphia, Pennsylvania 19104, United States

⁷Department of Physics and Astronomy, University of Pennsylvania, Philadelphia, Pennsylvania, 19104, United States

* Corresponding authors: dmj@seas.upenn.edu, engheta@seas.upenn.edu, jonghwankim@postech.ac.kr

Abstract

Hyperbolic media enable unique optical phenomena including hyperlensing, negative refraction, enhanced photonic density of states (PDOS), and highly confined polaritons. While most hyperbolic media are artificially engineered metamaterials, certain natural materials with extreme anisotropy can exhibit hyperbolic dispersion. Here, we report the first observation of natural hyperbolic dispersion in hexagonal boron nitride (hBN) in the deep-ultraviolet (DUV) regime, induced by strong, anisotropic exciton resonances. Using imaging spectroscopic ellipsometry (ISE), we characterize the complex dielectric function along in-plane and out-of-plane directions down to 190 nm (6.53 eV), revealing a type-II hyperbolic window in the DUV regime. This hyperbolicity supports hyperbolic exciton polaritons (HEP) with high directionality and slow group velocity. Our findings establish hBN as a promising platform for nanophotonic applications in the technologically significant DUV spectral range.

Introduction

Nanoscale light manipulation is crucial for developing next-generation nano-optical devices for sensing¹, waveguiding², and imaging³. Hyperbolic media, characterized by permittivities of opposite sign along different crystal axes (e.g., $Re(\epsilon_{\parallel}) \times Re(\epsilon_{\perp}) < 0$), have attracted significant attention due to their ability to support large wavevectors, enabling extreme sub-diffraction light confinement and large photonic density of states (PDOS)^{4,5}. Since hyperbolic dispersion requires large anisotropy, it is typically achieved in artificially made hyperbolic metamaterials (HMMs)^{3,6-9}, which are realized by subwavelength multilayer stacks of alternating dielectric and metallic films, exhibiting hyperbolic dispersion because it heavily relies on the plasmonic resonance of the metal layers⁴. These HMMs exhibit an open isofrequency surface, supporting the propagation of high-momentum waves and enabling unique phenomena like negative refraction¹⁰, sub-diffraction imaging via hyperlensing^{3,8,9}, and substantial enhancement of the Purcell factor¹¹.

Van der Waals (vdW) two-dimensional (2D) materials exhibit inherent high anisotropy along the out-of-plane direction due to their layered structure. This pronounced anisotropy is a key prerequisite for hyperbolic dispersion¹²⁻¹⁴. Moreover, the pronounced anisotropy of certain vdW 2D crystals gives rise to strongly direction-dependent resonances—phonons, plasmons, and excitons—which profoundly impact their dielectric response¹⁵. Prior results have revealed hyperbolic behavior originating from the anisotropic resonances of phonons in α -MoO₃¹⁶ and hexagonal boron nitride (hBN)¹⁷, plasmons in WTe₂¹⁸, and excitons in monolayer black phosphorus (BP)¹⁹ and chromium sulfide bromide (CrSBr)²⁰ at cryogenic temperatures.

Natural hyperbolic media support hybrid electromagnetic modes (hyperbolic polaritons) that enable broadband, deeply sub-diffractive confinement with strongly directional propagation. Natural hyperbolic phonon polaritons were first observed in hBN crystals experimentally by near-field measurements in the mid-infrared (MIR)²¹. Since then, various hyperbolic polaritons driven by phonons, plasmons, and excitons have been demonstrated across many material platforms. Their extreme mode confinement, high PDOS, and directional energy flow promise new capabilities in sub-diffraction imaging, near-field focusing, and nanophotonic applications¹⁵. While phonon- and plasmon-mediated hyperbolicity has been extensively explored, exciton-induced hyperbolicity remains relatively rare, as it requires materials with exceptionally strong excitonic resonances with extreme anisotropy.

hBN is a well-known vdW polar dielectric exhibiting hyperbolic dispersion in the MIR regime due to anisotropic phonon resonances^{15,21}. It has also attracted attention as an excitonic material due to its strong emission in the deep-ultraviolet (DUV) regime (around 180 ~ 300 nm, 4.13 ~ 6.89 eV)²². Even though the fundamental bandgap of hBN is an indirect bandgap (K→M point) in the DUV regime, as proved by the two-photon excitation spectroscopy²³, it also has a direct transition near ~ 6.1 eV at the K valley, supported by numerous density-functional theory (DFT) calculations and experiments²⁴⁻²⁶. Strong in-plane covalent bonding and weak out-of-plane van der Waals interactions create tightly bound 2D excitons with the large binding energy, E_b ~ 700 meV, for the lowest exciton^{24,27-29}. In addition, the electronic flatband of hBN in the Brillouin zone facilitates strong light-matter interaction²⁴.

We report the first observation of natural hyperbolic dispersion in hBN, arising from its anisotropic strong exciton resonances in the DUV regime. Using imaging

spectroscopic ellipsometry (ISE), we characterize the complex refractive index and exciton resonance properties of hBN along in-plane (\parallel) and out-of-plane (\perp) directions. hBN shows pronounced exciton oscillator strength in the in-plane direction compared to the out-of-plane direction, creating a hyperbolic window in the DUV regime. This hyperbolicity enables a transition in the isofrequency contour from elliptic (closed) to hyperbolic (open) shape, supporting hyperbolic exciton polaritons (HEP) with high directionality and confinement^{15,20}. Our findings enable light manipulation at the nanoscale in the DUV regime, which is critical for extreme-resolution photolithography using 193 nm ArF excimer lasers and DUV nonlinear optics.

Results and Discussion

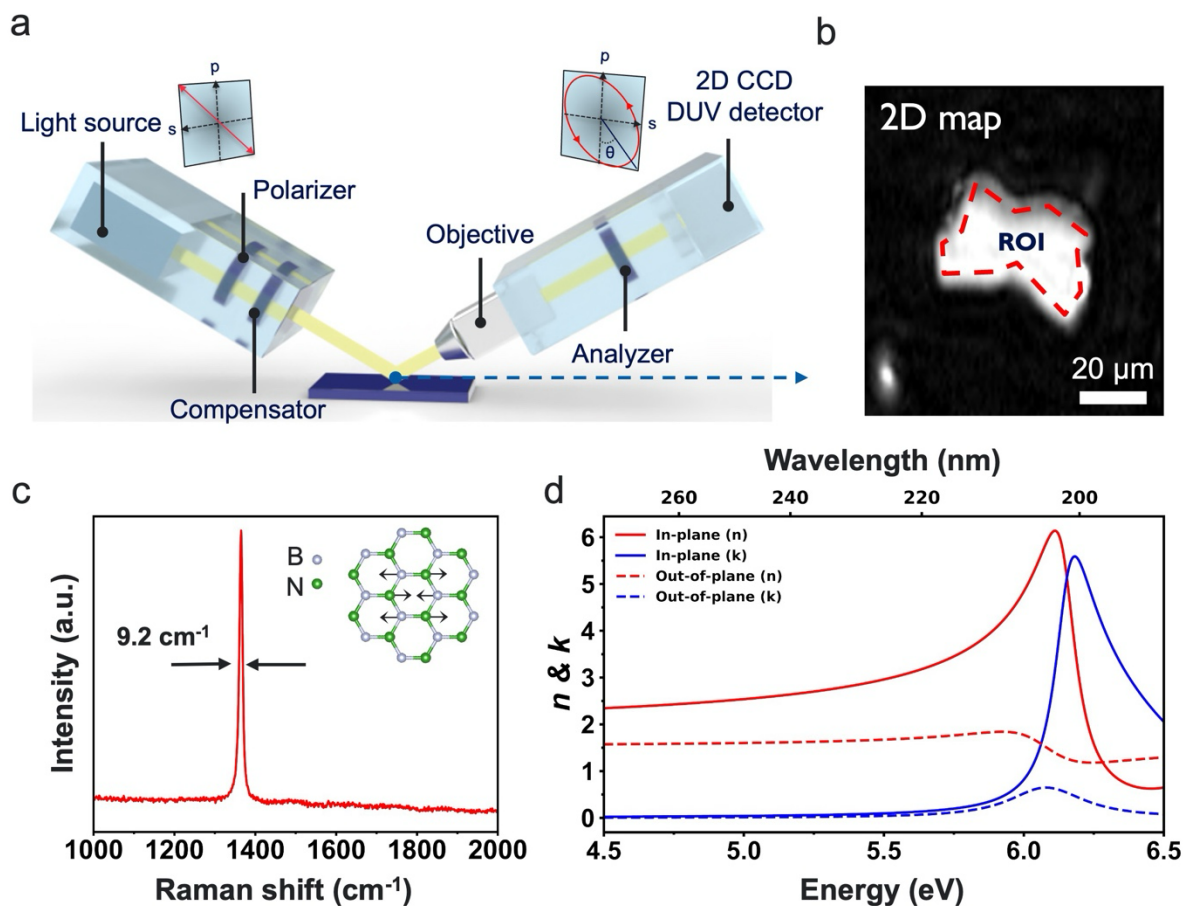


Figure 1. Imaging spectroscopic ellipsometry measurement of hBN. (a) Schematic illustration of ISE. Unlike conventional spectroscopic ellipsometry, imaging ellipsometry uses a high-resolution ($\sim 1 \mu\text{m}$) 2D charge-coupled device (CCD) detector with an objective lens ($7\times$) to map Ψ and Δ values, allowing the extraction of optical properties from even small flakes. (b) Example of the mapped image data of a small hBN flake using ISE. (c) Raman spectrum obtained from measured hBN shows a clear E_{2g} resonance with a narrow FWHM, demonstrating the high quality of the measured hBN. (d) Refractive index (n) and extinction coefficient (k) of hBN along the different optical axes (in-plane (\parallel) and out-of-plane (\perp)) showing strong excitonic features of hBN. These extracted values from ISE are in agreement with prior measurements using synchrotron radiation and inelastic electron scattering^{26,30}.

While hBN's optical properties in the DUV have been widely studied, its electronic band structure calculation from the *ab initio* approach and its transitions by inelastic electron scattering (IES) measurement^{24,26,28,31}, there are very few spectroscopic-ellipsometry measurements that provide sensitive measurements^{14,30}. Particularly, refractive indices resolved separately along the in-plane and out-of-plane directions are rare, yet they provide indispensable insight into the material's anisotropy and hyperbolic nature in the DUV excitonic regime. Recent ellipsometry studies have revealed a high refractive index and strong birefringence of hBN in the UV regime (around 250 nm), although they did not capture the excitonic resonance in the DUV regime¹⁴. We first characterize the excitonic features and refractive index of hBN along in-plane and out-of-plane directions using ISE down to the DUV to NIR regimes (190 ~ 1000 nm, 1.24 ~ 6.53 eV). First, we prepare the hBN sample using mechanical exfoliation with tape and transfer it onto the target substrate (See Methods). We chose the substrate Al₂O₃ which has a wide bandgap to increase the signal intensity and fidelity in DUV regime. When linearly polarized light is incident on a sample, strong excitonic resonances in its dielectric function cause variations in the Fresnel reflection coefficients r_p and r_s , consequently changing the ellipsometry parameters Ψ (the amplitude ratio) and Δ (the phase difference) with high sensitivity, enabling exciton behavior characterization³². Furthermore, obliquely incident light distinguishes a sample's electromagnetic response parallel to the surface from that perpendicular to it (Fig. 1a)³². As shown in Fig. 1b, an exfoliated hBN flake was characterized by ISE. The ~ 1 μm lateral resolution of our ISE allows detailed optical properties (Ψ and Δ) map data to be acquired as a function of incidence angle and wavelength on the small flakes that are inaccessible with conventional spectroscopic ellipsometry. The Raman spectrum of hBN exhibits a sharp peak at 1370 cm^{-1} with a full width at half maximum (FWHM) of approximately 9.2 cm^{-1} , indicative of the material's high quality and the characteristic E_{2g} vibrational mode, corresponding to the in-plane stretching of B and N atoms, as illustrated in the inset (Fig. 1c)²⁷. This minimal structural disorder and low strain are essential for preserving strong excitonic resonances. We obtain the Ψ and Δ (Supporting information (SI) Fig. S1) map and make the optical model using multiple Lorentz oscillator models to capture the exciton resonance behavior in hBN (see SI Note 1)³². Because hBN is uniaxial material, we modelled the in-plane and out-of-plane dielectric functions independently using distinct multiple Lorentz oscillator models. To improve the reliability of the results, multiple hBN thicknesses are measured at various incidence angles between 40° and 70° with respect to the sample's surface. The large variation in incidence angle, and thick flakes, yields a strong out-of-plane signal allowing us to determine the uniaxial dielectric function with high fidelity. The multiple Lorentz oscillator model captures the interband transitions in hBN along different optical axes with high accuracy, showing strong agreement with the experimentally obtained Ψ and Δ values across various incident angles and hBN thicknesses (SI Fig. S2). The measured hBN's complex refractive index is shown in Fig. 1d along the in-plane (\parallel) and out-of-plane (\perp) directions. In the in-plane direction, hBN shows a strong exciton oscillation around 6.14 eV with a pronounced extinction coefficient (k), corresponding to the direct $\pi \rightarrow \pi^*$ transition at the K band in reciprocal space. This observation aligns well with the theoretical electronic band calculation using the *ab initio* (GW+BSE) method^{24,28} as well as prior experimental measurements using synchrotron radiation³⁰ and inelastic electron scattering²⁶. Although bulk hBN possesses an indirect bandgap, phonon-assisted (indirect) optical transitions are essentially absent from the measured spectra since their oscillator strength is orders of magnitude weaker than that of the dominant excitonic resonance^{33,34}. Furthermore,

the substantial refractive index ($n \sim 2.5$ at 250 nm), while the loss remains low, due to strong excitons at the UV and DUV regime of hBN shows appliance to the UV optics primarily relied on the low refractive index materials such as fused silica (SiO_2 , $n \sim 1.5$ at 250 nm)³⁵ and magnesium fluoride (MgF_2 , $n \sim 1.4$ at 250 nm)³⁶. On the other hand, hBN exhibits the interband transition along the out-of-plane direction with a small extinction coefficient (k) compared to that of the in-plane components due to its highly in-plane oriented exciton nature²⁷. This observation is well aligned with the previous literature²⁶, manifesting strong and anisotropic excitonic behavior, which induces hyperbolic dispersion, discussed later.

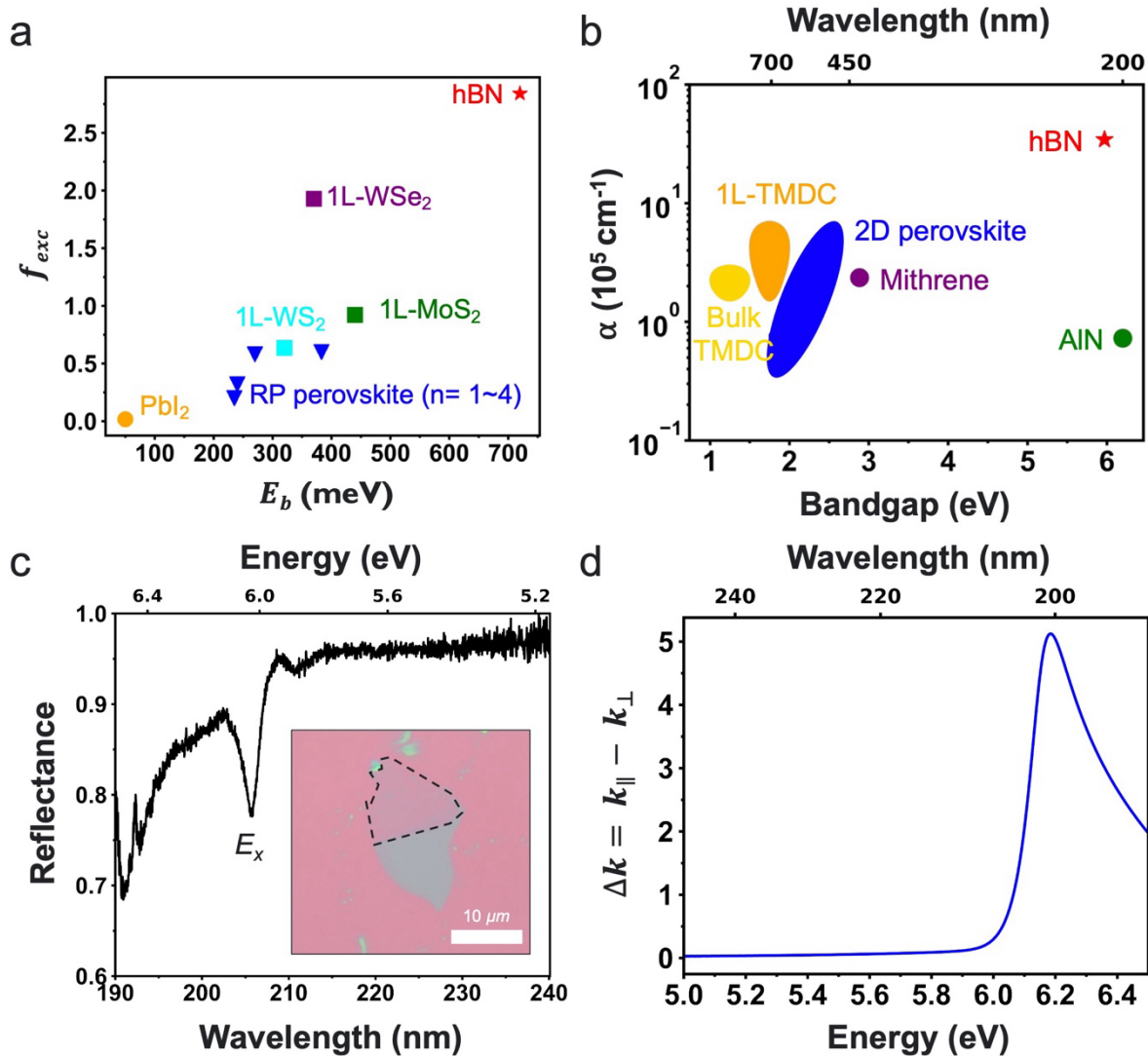


Figure 2. Exciton properties of hBN. (a) Comparison of exciton oscillator strength and exciton binding energy of various excitonic materials (hBN, monolayer TMDCs, 2D RP perovskite, and PbI_2), showing hBN's strong oscillator strength and exciton binding energy compared to the other excitonic materials. The exciton oscillator strengths are calculated using Eq. (1), and parameters such as interband oscillator strength, Bohr radius, and E_b are adapted from prior literature^{19,28,37-42}. (b) Comparison of the absorption coefficient of various excitonic (hBN, Bulk and monolayer of TMDCs (MoS_2 , MoSe_2 , MoTe_2 , WSe_2 , and WS_2), 2D RP and DJ perovskites, mithrene, and AlN)^{41,43-47}, illustrating significant absorption coefficient due to the tightly bound excitons in hBN (c) Reflectance spectrum (R_{hBN}/R_{Al}) in a 5L-hBN/Al structure, demonstrating the high absorbance from the thin hBN layer due to strong exciton resonance. The reflectance dips around 190 nm (6.53 eV) are originated from strong

absorption of air. Inset shows image of thin hBN flake on a Si/SiO₂ substrate before the pick-up transfer. Note that the thickness of hBN was determined by the ISE measurement (SI Fig. S4) (d) Calculated linear dichroism ($\Delta k = k_{\parallel} - k_{\perp}$) as a function of photon energy, revealing a large dichroism originated from anisotropic exciton resonances.

Since the excitonic response critically governs the optical properties and potential hyperbolic behavior of 2D materials, we investigate the strong excitonic feature of hBN to analyze the origin of hyperbolicity by evaluating its exciton oscillator strength from the interband oscillator strength in ellipsometry measurements (Fig. 2a). Generally, because 2D materials strongly support confined excitons in two dimensions with reduced dielectric screening, they exhibit significantly larger E_b and strong oscillator strengths compared to their bulk counterparts⁴⁸. The exciton oscillator strengths (f_{exc}) can be calculated using the simple formulation proposed by *Ishihara et al.*⁴².

$$f_{exc} = \frac{2fS_0}{\pi a_{2D}^2} \text{ or } \frac{2fV_0}{\pi a_{3D}^2} \quad (1)$$

, where f is the interband oscillator strength, S_0 (V_0) is a unit-cell area (volume), and a_{2D} (a_{3D}) is the material's 2D (3D) Bohr radius. Since a smaller exciton Bohr radius is advantageous for the strong oscillator strength, f_{exc} shows an inversely square (cubic) proportional relation to Bohr radius, respectively. Tightly bound hBN excitons exhibit a small Bohr radius²⁷, resulting in a pronounced f_{exc} and E_b compared to the well-known highly excitonic materials, such as monolayer transition metal dichalcogenides (TMDCs), and 2D Ruddlesden-Popper (RP) perovskites. Monolayer TMDCs exhibit a large oscillator strength, although it is slightly smaller than that of hBN. Consequently, several studies have reported hyperbolic dispersion of 2D vdW materials under specific conditions where excitonic resonances are enhanced, such as at low temperatures, highlighting the critical role of excitons in governing hyperbolicity^{20,49}. Furthermore, RP perovskites exhibit a near-hyperbolic dispersion around exciton resonance, characterized by $Re(\epsilon_{\parallel})$ approaching zero while $Re(\epsilon_{\perp})$ remains positive, suggesting that true hyperbolicity could potentially emerge at low temperatures⁴¹. For comparison, PbI₂, which does not support strong excitonic effects, exhibits small values of f_{exc} and E_b , indicating that excitons play an important role in the material's optical properties⁴². Fig. 2b shows the absorption coefficient, $\alpha = 4\pi k/\lambda$, of various well-known excitonic materials including hBN (Bulk and monolayer TMDCs, 2D RP and Dion-Jacobson (DJ) perovskites, mithrene (AgSePh), and AlN). The giant excitonic oscillator strength of hBN enables a strong absorption peak around the exciton energy approximately $3.5 \times 10^6 \text{ cm}^{-1}$ (SI Fig. S3), which is consistent with the observation in Fig. 2a. Because exciton oscillator strength scales with optical absorption, monolayer TMDCs, where reduced dielectric screening enhances excitonic features such as E_b and f_{exc} , exhibit more significant absorption coefficients than their bulk counterparts. Notably, hBN's tightly bound exciton gives rise to absorption coefficients nearly an order of magnitude higher than other excitonic semiconductors. Even compared to wide-bandgap AlN, whose band edge lies similarly in the DUV, hBN's excitonic resonance boosts its absorption by approximately two orders of magnitude, underscoring the dramatic impact of its bound excitons. Therefore, exciton dominates the optical responses in the DUV regime of hBN.

To probe the strong excitonic response, we measure the reflectance spectrum of thin hBN (5 layers) on an Al substrate in the DUV regime. The spectrum reveals pronounced absorption near the exciton energy, as shown in Fig. 2c. Notably, most of the observed absorption originates from the hBN layer rather than the underlying Al substrate, as confirmed by the transfer matrix method (TMM)^{50,51} calculation results (SI Fig. S5). More importantly, these strong excitons only exist along the in-plane direction, resulting in a large dichroism ($\Delta k = k_{\parallel} - k_{\perp}$) around 5, which reflects the difference in absorption properties along different optical axes, a prerequisite for natural hyperbolicity. Along with dichroism, hBN shows large birefringence in the DUV regime since dichroism and birefringence are related under the Kramers-Kronig relation (SI Fig. S6)³². In addition, the large birefringence of hBN, even well below the band gap where loss is low, makes it uniquely suited for UV and DUV polarization optics; an attribute few other materials can match¹⁴.

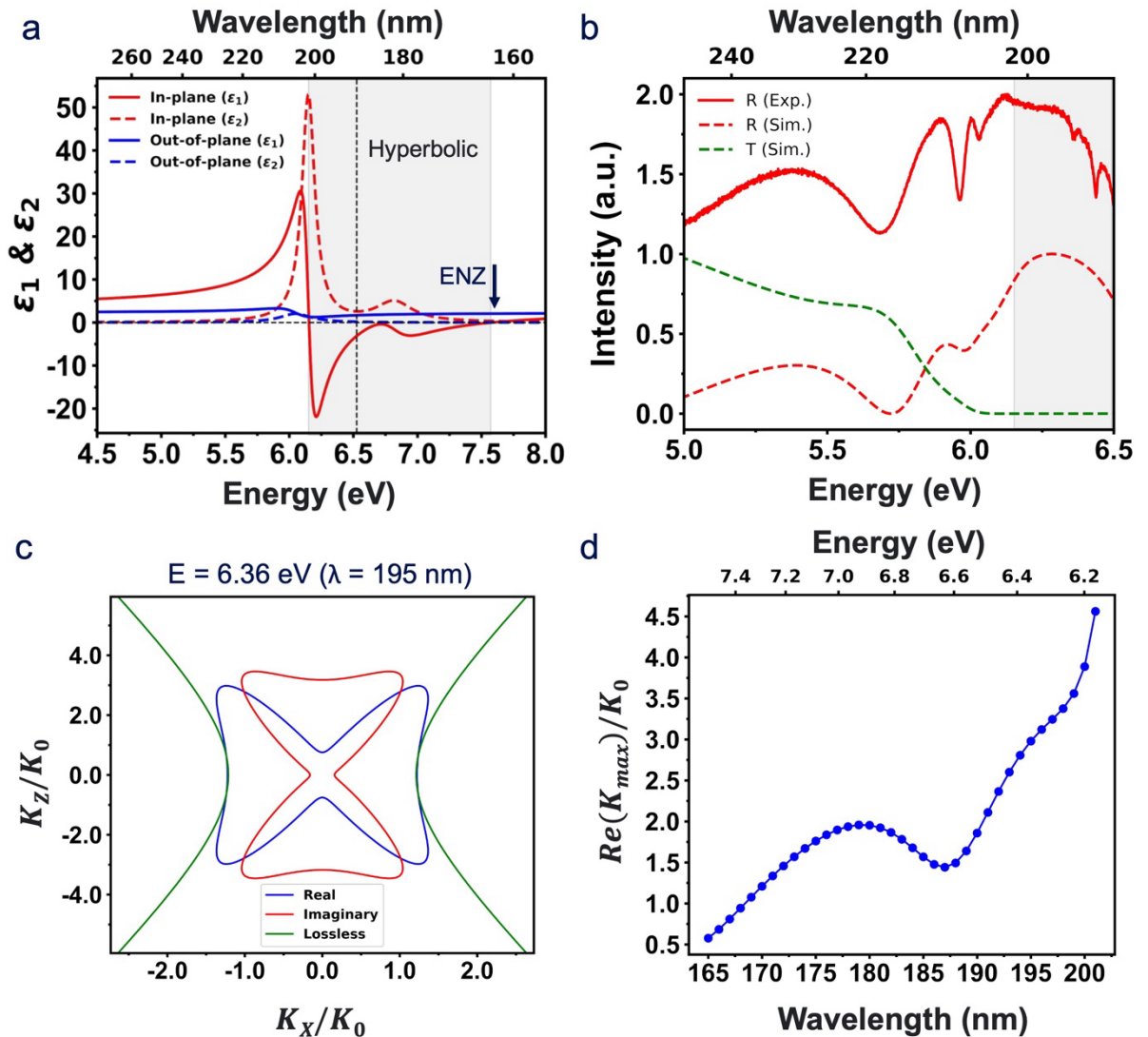


Figure 3. Natural hyperbolic dispersion in hBN. (a) Complex permittivities ($\epsilon = \epsilon_1 + i\epsilon_2$) of hBN along different optical axes (in-plane (\parallel) and out-of-plane (\perp)) indicating apparent hyperbolic dispersion (grey shaded area) in the DUV regime with ENZ point. The permittivities are extrapolated based on the multiple Lorentz oscillator model obtained from the ISE measurement above (below) 6.53 eV (190 nm). Dashed vertical line represent the boundary

between experimental and extrapolated regime. (b) Measured (solid red curve) and simulated (dotted red curve) reflectance, along with simulated transmittance (dotted green curve), from a 63 nm hBN sample on an Al₂O₃ substrate in the DUV regime, showing the Reststrahlen (grey shaded area) with highly reflective properties. (c) Isofrequency surface of hBN at 6.36 eV (195 nm) for TM plane wave with real loss (red and blue curves) and no loss (green curve), showing clear hyperbolic dispersion arising from different signs of permittivities along different optical axes. (d) The max wavevector can be supported by the hBN as a function of wavelength (photon energy), reaching approximately ~ 4.6 around the exciton resonance.

As shown in Fig. 3a, we plot the complex permittivity ($\varepsilon = \varepsilon_1 + i\varepsilon_2$) of hBN, where $\varepsilon_1 = n^2 - k^2$ and $\varepsilon_2 = 2nk$, along both its in-plane and out-of-plane directions. The permittivity was directly retrieved from ISE measurements down to 190 nm (6.53 eV), a measurable wavelength regime from our tool. To extend our model to shorter wavelengths (~ 155 nm, ~ 8.0 eV), we extrapolated the data using a multi Lorentz oscillator model (See SI Note 1) obtained from multiple samples and incidence angles. Since the higher energy electron transition above 6.53 eV is out of range from our tool, we adapted the previous synchrotron study to capture the high energy interband transitions (e.g., $\pi \rightarrow \pi^*$ transition and $\sigma \rightarrow \sigma^*$ transition)³⁰. Due to its pronounced anisotropic excitonic resonances, hBN supports a well-defined DUV type-II hyperbolic window around 6.17 eV \sim 7.56 eV (164 nm \sim 201 nm), where $\varepsilon_{1,\parallel} < 0$ and $\varepsilon_{1,\perp} > 0$. We further identify an intrinsic epsilon-near-zero (ENZ) wavelengths in hBN near 7.56 eV, where the losses are minimal. These naturally occurring hyperbolicity and ENZ points promise new opportunities for DUV nanophotonic device engineering and quantum-optical applications^{52,53}. In its type-II hyperbolic regime, hBN exhibits a metallic in-plane permittivity while maintaining a dielectric response along the out-of-plane direction, a condition that underpins the formation of its Reststrahlen band. Our measured and simulated reflectance spectrum from hBN (63 nm) on Al₂O₃ substrate exhibit the high reflectivity plateau of the hBN's Reststrahlen band (grey-shaded region), an intrinsic consequence of its hyperbolic dispersion (Fig. 3b)^{17,24}. The Reststrahlen band is observed in hBN flakes of various thicknesses (see SI Fig. S7a). In addition, the simulated transmission spectrum dips to near zero, confirming that electromagnetic waves cannot propagate normally through the hBN in this band except as evanescent/high-k modes. In the strong-response regime dominated by coherent radiative decay in the Reststrahlen band, hBN exhibits highly reflective behavior. However, as the thickness decreases and the hBN approaches the optically thin limit, a weak-response regime governed by damping emerges, where the broad Reststrahlen band transitions into a single resonance peak (SI Fig. S7b)⁵⁴. The Reststrahlen band shows a highly reflective nature for the wide range of incident angles in the strong response regime (SI Fig. S7c).

The hyperbolic features are manifested only under transverse-magnetic (TM)-polarized light, as it probes both in-plane and out-of-plane dielectric responses. In contrast, transverse-electric (TE)-polarized light is sensitive only to the in-plane permittivity and may not exhibit hyperbolic behavior. For the TM plane wave, Maxwell's equation yields a dispersion relation: $\frac{k_x^2}{\varepsilon_{1,\perp}} + \frac{k_z^2}{\varepsilon_{1,\parallel}} = k_0^2$, where $k_0 = \frac{\omega}{c}$ is the free space wavevector, and k_x and k_z are the wavevectors in the x-plane and z-plane,

respectively. Based on the dispersion relation, Fig. 3c shows the clear hyperbolic dispersion of hBN at 6.36 eV (195 nm) for each lossy (red and blue) and lossless (green) case, while hBN exhibits an elliptical dispersion outside the hyperbolic region as expected (SI Fig. S8). The anisotropic excitonic resonance gives rise to the hyperbolic dispersion, supporting highly confined light and large PDOS, enabling the formation of hyperbolic polaritons discussed later^{15,20,55}. In an ideal, lossless hyperbolic medium, the dispersion relation admits modes with infinitely large wavevectors in theory, formally yielding an infinite PDOS. In practice, however, material absorption introduces damping that imposes a finite cutoff on the maximum supported k-vector, resulting in a closed isofrequency surface⁵⁶, as shown in Fig. 3c. Thus, it becomes essential to quantify the impact of absorption, especially in regimes where hyperbolic dispersion is driven by exciton resonances, since these same resonances impart strong intrinsic damping. Over hBN's hyperbolic band, we compute the largest wavevector the material can support as a function of photon energy (wavelength). Approaching the exciton resonance, hBN's hyperbolic bands extend to larger wavevectors, albeit with rising absorption. SI Fig. S9 compares the loss-inclusive isofrequency contours at multiple photon energies (wavelength): as one approaches the exciton resonance (~ 6.14 eV), the real isofrequency surface expands (indicating larger wavevector) while the imaginary isofrequency surface grows simultaneously, indicating increased damping near the resonance. In its most extreme hyperbolic regime, hBN reaches $\text{Re}(K_{max})/K_0 \sim 4.6$ (Fig. 3d). Additionally, the enlarged wavevector space within hBN's hyperbolic band significantly enhances the PDOS, which is calculated by the Green's functions, resulting in an enhanced spontaneous emission rate, as quantified by the Purcell factor shown in the SI Fig. S10^{4,57}.

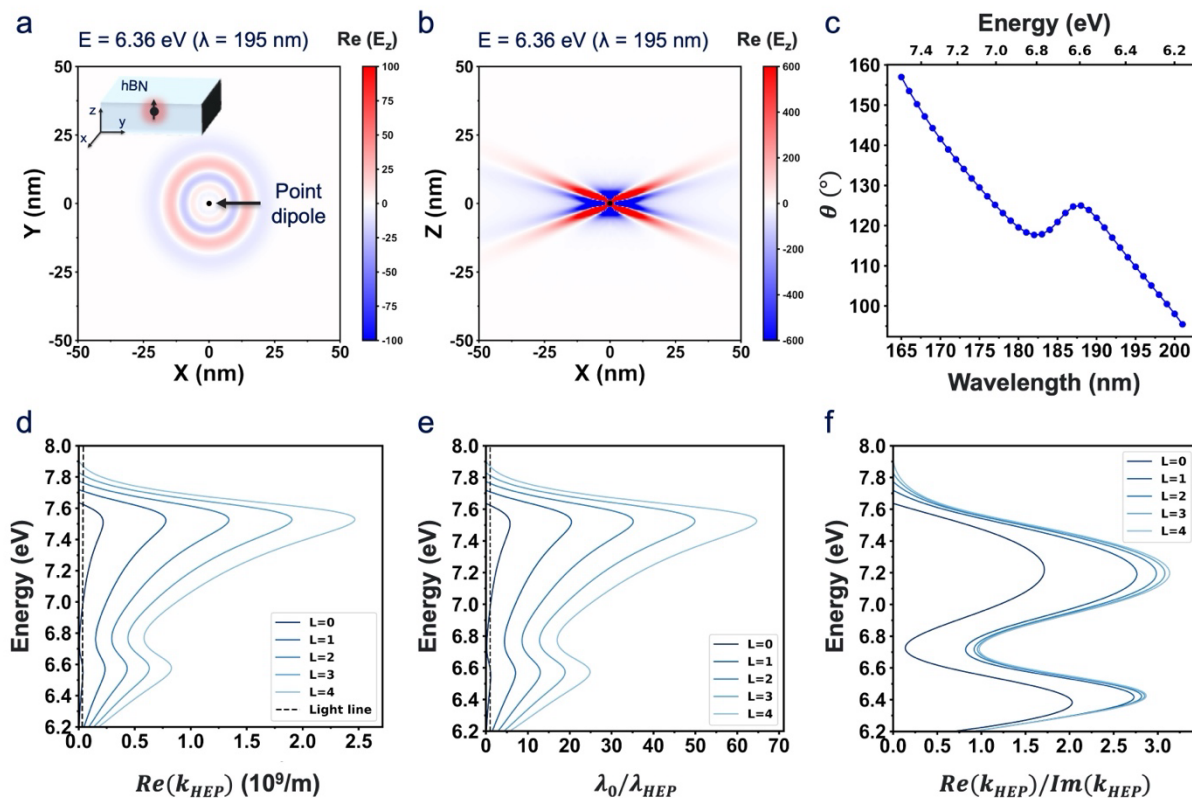


Figure 4. HEP propagation in hBN slab. Numerically simulated near-field wave propagation at 6.36 eV (195 nm) using finite-difference time-domain (FDTD) simulations, launched by a

point dipole oriented along the Z-axis, is shown in (a) the in-plane (XY) direction, revealing isotropic and radial propagation, and (b) the out-of-plane (XZ) direction, exhibiting the highly directional wave propagation due to the hyperbolic dispersion. (c) Wave propagation angle as a function of photon energy (wavelength). (d) The HEP's analytical dispersion relation as a function of an in-plane wavevector up to L=4 mode, where d_{hBN} is 10 nm, showing the highly confined nature of HEP. Calculated figure of merits: (e) Confinement factor λ_0/λ_{HEP} and (f) Propagation loss properties ($Re(k_{HEP})/Im(k_{HEP})$) of HEP as a function of incident photon energy, showing highly confined propagation characteristic.

We further investigate the highly confined HEP originating from hyperbolic dispersion. The numerically simulated wave launched by a point source oriented along the z-axis, as illustrated in the inset of Fig. 4a, displays a circularly shaped radial wave propagation at 6.36 eV (195 nm) in the XY plane. Since radiation in the XY plane consists solely of the E_z component, governed exclusively by a positive ε_{\perp} , the resulting radiation pattern exhibits the symmetric propagation shown in Fig. 4a. In contrast, the radiation pattern in the XZ plane comprises two components (E_x and E_z), allowing the field to probe the hyperbolic dispersion. Consequently, a point source excitation in a type-II hyperbolic medium produces a sharply defined hyperbolic radiating pattern from the origin in the XZ planes (Fig. 4b), which is consistent with the isofrequency surface at 6.36 eV (195 nm) in reciprocal space in Fig. 3c. On the other hand, the point source launched at 4.96 eV (250 nm), which is outside of the hyperbolic window, does not show directional propagation as can be expected from its isofrequency contour (SI Fig. S11). Since HEP supports large momentum, they are difficult to excite via direct free-space incidence in the far field¹. Thus, using a high-index prism such as the Otto and Kretschmann configuration under TM-polarized illumination enables efficient coupling to these high-k modes (SI Fig. S12)⁵⁸.

This hyperbolic dispersion enables highly directional propagation and high-electric field confinement of HEP in the near field, demonstrating high tunability of the wave on the nanoscale, in contrast to elliptical dispersion materials where energy spreads across the plane^{15,59}. In addition, HEP exhibits directional propagation depending on the frequency, and the propagation angle (θ), the angle between the Poynting vector and the z axis, can be approximately calculated by Eq. (2)⁶⁰:

$$\theta(\omega) = \pi/2 - \tan^{-1}(\sqrt{\varepsilon_{\perp}(\omega)}/i\sqrt{\varepsilon_{\parallel}(\omega)}) \quad (2)$$

In this regime, polaritons can only propagate at specific angles determined by the anisotropy of the material. The propagation angle (θ) decreases from 157° to 95° ($\Delta\theta \cong 62^\circ$) within the hyperbolic window as photon energy decrease (wavelength increases) (Fig. 4c). Simulated wave propagation in the XZ plane as a function of photon energy exhibits pronounced directionality, in agreement with the calculations shown in Fig. 4c. (SI Fig. S13). We analytically solve the HEP dispersion relation for TM modes, in the thin hBN slab following the general equations for the TM polariton mode given by Eq. (3)⁶¹:

$$k_{HEP} = \frac{i}{d_{hBN}} \sqrt{\frac{\varepsilon_{\perp}}{\varepsilon_{\parallel}}} [2 \tan^{-1} \left(i \frac{1}{\sqrt{\varepsilon_{\perp} \varepsilon_{\parallel}}} \right) + \pi L] \quad (3)$$

, where k_{HEP} is the x component of the wavenumber, d_{hBN} is the thickness of the hBN slab and $L = 0, 1, 2 \dots$ are integers indicating the higher order mode. The analytical dispersion relation derived from Eq. (3) clearly reveals the HEP mode, which carries a larger momentum than that of a free-space photon, where the dashed line represents the light line (Fig. 4d). As expected for the hyperbolic polariton, the HEP's dispersion relation exhibits an increasing momentum as mode order increases. In addition, the group velocity ($v_g = \partial\omega/\partial k_{HEP}$), the slope of the dispersion curve, decreases with increasing momentum, reflecting the slow group velocity and strong spatial confinement of higher-order modes¹⁷. We extract the commonly used figure of merits for the polariton: the confinement factor (λ_0/λ_{HEP}), where λ_0 is the free-space wavelength, and propagation figure of merit of HEP, defined as $Re(k_{HEP})/Im(k_{HEP})$ ^{55,62}. Fig. 4e shows the confinement factor depending on the mode order, showing the highly confined nature ($\lambda_0/\lambda_{HEP} > 1$) of HEP with an increase in confinement as the mode order increases. For the L=0 mode, the confinement factor reaches approximately 5.7, which is comparable to the values observed in exciton-polaritons in WSe₂⁶³. In addition, the confinement factor reaches values exceeding 10 for higher-order modes, underscoring the extreme subwavelength confinement enabled by the hyperbolic dispersion in hBN. As shown in Fig. 4f, higher propagation figure of merit values indicates reduced relative propagation losses of HEP. This suggests that, despite their inherently large momentum, HEP can still propagate appreciable distance (~20 nm) before significant attenuation occurs^{49,61}. Furthermore, the value of propagation figure of merit increases with mode order, reflecting improved loss-performance characteristics in higher-order modes. The calculated propagation length along the direction corresponding to the maximum real part of the wavevector is approximately 20 nm (SI Fig. S14)⁵⁶.

Conclusion

We report the emergence of natural hyperbolic dispersion in hBN arising from strong and anisotropic excitonic resonances in the DUV regime. Using ISE with micron resolution, we extract the complex dielectric functions along both in-plane and out-of-plane directions, revealing a clear type-II hyperbolic window induced by excitonic anisotropy. We identify the Reststrahlen band originating from hyperbolicity through reflectance spectroscopy, showing good agreement with numerical calculations. Moreover, this hyperbolic dispersion supports highly confined polaritonic modes with large momenta, slow group velocities, and enhanced photonic density of states. We confirm this through numerical simulations and analytical modeling of the HEP dispersion relation, showing strong confinement factors and moderate propagation figures of merit. These findings establish hBN as a promising candidate for DUV nanophotonics, providing a pathway toward next-generation polaritonic devices for sub-diffraction imaging, DUV lithography, and quantum optical applications.

Methods

Sample preparation

The exfoliated hBN sample has prepared using two methods, direct transfer and pick-up transfer. For the direct transfer, the bulk hBN was exfoliated using blue tape and then directly dry transferred on top of the target substrate. For the pick-up transfer,

mechanically exfoliated hBN flakes were picked up using a dry transfer method⁶⁴ with polycarbonate (PC) /polydimethylsiloxane (PDMS) and subsequently transferred onto the target substrate. After the transfer, the samples were immersed in chloroform for 1 hour to dissolve the PC film.

Imaging spectroscopic ellipsometry

Imaging ellipsometry measurements for determining the dielectric function were performed using the Accurion EP4 system (Park Systems) over the 190–1000 nm spectral range. A 7× objective lens was used for measurements in the DUV regime. Multi-angle incidence measurements were conducted over an angular range of 40° to 70°. The measured mapping data were analyzed using the EP4 model and DataStudio software provided by the EP4 system.

Raman characterization

Raman spectra were acquired using a Horiba LabRam HR Evolution confocal microscope, with a 600 grooves/mm grating and a 633 nm continuous-wave (CW) laser for excitation. The signal was detected using a CCD detector.

Reflectance measurements

Reflectance measurements were performed using a Hamamatsu deuterium lamp as the light source. The DUV light was guided into a home-built confocal microscopy set-up, which was constructed using DUV-enhanced aluminum mirrors, a DUV-enhanced reflective objective with a numerical aperture of 0.4, CaF₂ lenses, and a CaF₂ beam splitter. A 4f optical system was implemented, and a size-tunable aperture was placed at the image plane to spatially filter the reflected signal, thereby isolating the reflectance from the hexagonal boron nitride samples while blocking contributions from the underlying substrate. The reflected light was guided into a spectrometer and detected using an electrically cooled Si CCD camera.

Optical simulations

Electric field profiles in the near field were calculated using FDTD simulations performed with the commercial software Lumerical. Theoretical reflectance and absorbance are computed using the TMM with homemade Python code^{50,51}. The refractive index of hBN was determined through imaging ellipsometry, while those of Al₂O₃⁶⁵ and Al⁶⁶ were adopted from previously reported literature values.

Author Contribution

D.J. supervised and acquired funding for the project. D.J. and B.C. conceived and designed the experiment. B.C. performed the ellipsometry measurements and conducted the data fitting. B.C. performed the optical simulations and calculations in discussion with D.J., N.E., and J.L. W.C. fit preliminary ellipsometry data. K.Y. fabricated samples. S. J. and H.C. performed the reflectance measurement under the supervision of J. K. B.C. and D.J. wrote the manuscript with inputs from all authors. All authors discussed the results and revised the manuscript

Acknowledgement

D. J., B.C., and J.L. acknowledge support from the Office of Naval Research Young Investigator Award, Metamaterials Program (N00014-23-1-203). This work was

carried out in part at the Singh Center for Nanotechnology, which is supported by the NSF National Nanotechnology Coordinated Infrastructure Program under Grant NNCI-2025608. J.K. acknowledges the support from the Institute for Basic Science (IBS), Korea under Project Code IBS-R014-A1 and the National Research Foundation of Korea grants (NRF-2023R1A2C2007998). N. E. acknowledges partial support from the US Air Force Office of Scientific Research (AFOSR) Multidisciplinary University Research Initiatives (MURI) program with grant # FA9550-21-1-0312 and AFOSR grant # FA9550-23-1-030.7

References

- 1 Sreekanth, K. V. *et al.* Extreme sensitivity biosensing platform based on hyperbolic metamaterials. *Nature materials* **15**, 621-627 (2016).
- 2 Sternbach, A. *et al.* Programmable hyperbolic polaritons in van der Waals semiconductors. *Science* **371**, 617-620 (2021).
- 3 Liu, Z., Lee, H., Xiong, Y., Sun, C. & Zhang, X. Far-field optical hyperlens magnifying sub-diffraction-limited objects. *science* **315**, 1686-1686 (2007).
- 4 Poddubny, A., Iorsh, I., Belov, P. & Kivshar, Y. Hyperbolic metamaterials. *Nature photonics* **7**, 948-957 (2013).
- 5 Krishnamoorthy, H. N., Jacob, Z., Narimanov, E., Kretzschmar, I. & Menon, V. M. Topological transitions in metamaterials. *Science* **336**, 205-209 (2012).
- 6 Yang, X., Yao, J., Rho, J., Yin, X. & Zhang, X. Experimental realization of three-dimensional indefinite cavities at the nanoscale with anomalous scaling laws. *Nature Photonics* **6**, 450-454 (2012).
- 7 Lynch, J. *et al.* High-Temperature-Resilient Hyperbolicity in a Mixed-Dimensional Superlattice. *arXiv preprint arXiv:2503.16147* (2025).
- 8 Salandrino, A. & Engheta, N. Far-field subdiffraction optical microscopy using metamaterial crystals: Theory and simulations. *Physical Review B—Condensed Matter and Materials Physics* **74**, 075103 (2006).
- 9 Jacob, Z., Alekseyev, L. V. & Narimanov, E. Optical hyperlens: far-field imaging beyond the diffraction limit. *Optics express* **14**, 8247-8256 (2006).
- 10 Hoffman, A. J. *et al.* Negative refraction in semiconductor metamaterials. *Nature materials* **6**, 946-950 (2007).
- 11 Poddubny, A. N., Belov, P. A. & Kivshar, Y. S. Spontaneous radiation of a finite-size dipole emitter in hyperbolic media. *Physical Review A—Atomic, Molecular, and Optical Physics* **84**, 023807 (2011).
- 12 Choi, B. *et al.* Giant Optical Anisotropy in 2D Metal–Organic Chalcogenates. *ACS nano* **18**, 25489-25498 (2024).
- 13 Zhang, H. *et al.* Cavity-enhanced linear dichroism in a van der Waals antiferromagnet. *Nature Photonics* **16**, 311-317 (2022).
- 14 Grudinin, D. *et al.* Hexagonal boron nitride nanophotonics: a record-breaking material for the ultraviolet and visible spectral ranges. *Materials Horizons* **10**, 2427-2435 (2023).
- 15 Wang, H. *et al.* Planar hyperbolic polaritons in 2D van der Waals materials. *Nature communications* **15**, 69 (2024).
- 16 Ma, W. *et al.* In-plane anisotropic and ultra-low-loss polaritons in a natural van der Waals crystal. *Nature* **562**, 557-562 (2018).
- 17 Giles, A. J. *et al.* Ultralow-loss polaritons in isotopically pure boron nitride. *Nature materials* **17**, 134-139 (2018).
- 18 Wang, C. *et al.* Van der Waals thin films of WTe₂ for natural hyperbolic plasmonic surfaces. *Nature communications* **11**, 1158 (2020).
- 19 Wang, F. *et al.* Prediction of hyperbolic exciton-polaritons in monolayer black phosphorus. *Nature communications* **12**, 5628 (2021).
- 20 Ruta, F. L. *et al.* Hyperbolic exciton polaritons in a van der Waals magnet. *Nature communications* **14**, 8261 (2023).
- 21 Dai, S. *et al.* Tunable phonon polaritons in atomically thin van der Waals crystals of boron nitride. *Science* **343**, 1125-1129 (2014).
- 22 Watanabe, K., Taniguchi, T. & Kanda, H. Direct-bandgap properties and evidence for ultraviolet lasing of hexagonal boron nitride single crystal. *Nature materials* **3**, 404-409 (2004).
- 23 Cassabois, G., Valvin, P. & Gil, B. Hexagonal boron nitride is an indirect bandgap semiconductor. *Nature photonics* **10**, 262-266 (2016).
- 24 Elias, C. *et al.* Flat bands and giant light-matter interaction in hexagonal boron nitride. *Physical Review Letters* **127**, 137401 (2021).

- 25 Zunger, A., Katzir, A. & Halperin, A. Optical properties of hexagonal boron nitride. *Physical Review B* **13**, 5560 (1976).
- 26 Tarrío, C. & Schnatterly, S. Interband transitions, plasmons, and dispersion in hexagonal boron nitride. *Physical review B* **40**, 7852 (1989).
- 27 Cao, X., Clubine, B., Edgar, J., Lin, J. & Jiang, H. Two-dimensional excitons in three-dimensional hexagonal boron nitride. *Applied physics letters* **103** (2013).
- 28 Arnaud, B., Lebègue, S., Rabiller, P. & Alouani, M. Huge excitonic effects in layered hexagonal boron nitride. *Physical review letters* **96**, 026402 (2006).
- 29 Wirtz, L., Marini, A. & Rubio, A. Excitons in boron nitride nanotubes: dimensionality effects. *Physical review letters* **96**, 126104 (2006).
- 30 Artús, L. *et al.* Ellipsometry study of hexagonal boron nitride using synchrotron radiation: transparency window in the Far-UV. *Advanced Photonics Research* **2**, 2000101 (2021).
- 31 Sponza, L. *et al.* Direct and indirect excitons in boron nitride polymorphs: A story of atomic configuration and electronic correlation. *Physical Review B* **98**, 125206 (2018).
- 32 Fujiwara, H. *Spectroscopic ellipsometry: principles and applications*. (John Wiley & Sons, 2007).
- 33 Cannuccia, E., Monserrat, B. & Attacalite, C. Theory of phonon-assisted luminescence in solids: application to hexagonal boron nitride. *Physical Review B* **99**, 081109 (2019).
- 34 Paleari, F., PC Miranda, H., Molina-Sánchez, A. & Wirtz, L. Exciton-phonon coupling in the ultraviolet absorption and emission spectra of bulk hexagonal boron nitride. *Physical review letters* **122**, 187401 (2019).
- 35 Malitson, I. H. Interspecimen comparison of the refractive index of fused silica. *Journal of the optical society of America* **55**, 1205-1209 (1965).
- 36 Dodge, M. J. Refractive properties of magnesium fluoride. *Applied optics* **23**, 1980-1985 (1984).
- 37 Hill, H. M. *et al.* Observation of excitonic Rydberg states in monolayer MoS₂ and WS₂ by photoluminescence excitation spectroscopy. *Nano letters* **15**, 2992-2997 (2015).
- 38 He, K. *et al.* Tightly bound excitons in monolayer WSe₂. *Physical review letters* **113**, 026803 (2014).
- 39 Wang, G. *et al.* Exciton states in monolayer MoSe₂: impact on interband transitions. *2D Materials* **2**, 045005 (2015).
- 40 Blancon, J.-C. *et al.* Extremely efficient internal exciton dissociation through edge states in layered 2D perovskites. *Science* **355**, 1288-1292 (2017).
- 41 Song, B. *et al.* Determination of dielectric functions and exciton oscillator strength of two-dimensional hybrid perovskites. *ACS Materials Letters* **3**, 148-159 (2020).
- 42 Ishihara, T., Takahashi, J. & Goto, T. Optical properties due to electronic transitions in two-dimensional semiconductors (C_nH_{2n+1}NH₃)₂PbI₄. *Physical review B* **42**, 11099 (1990).
- 43 Jariwala, D., Davoyan, A. R., Wong, J. & Atwater, H. A. Van der Waals materials for atomically-thin photovoltaics: promise and outlook. *Acs Photonics* **4**, 2962-2970 (2017).
- 44 Ahuja, R. *et al.* Electronic and optical properties of lead iodide. *Journal of applied physics* **92**, 7219-7224 (2002).
- 45 Li, Y. *et al.* Measurement of the optical dielectric function of monolayer transition-metal dichalcogenides: MoS₂, MoSe₂, WS₂, and WSe₂. *Physical Review B* **90**, 205422 (2014).
- 46 Anantharaman, S. B. *et al.* Ultrastrong light-matter coupling in two-dimensional metal-organic chalcogenolates. *Nature Photonics*, 1-7 (2025).
- 47 Beliaev, L. Y., Shkondin, E., Lavrinenko, A. V. & Takayama, O. Thickness-dependent optical properties of aluminum nitride films for mid-infrared wavelengths. *Journal of Vacuum Science & Technology A* **39** (2021).

- 48 Chernikov, A. *et al.* Exciton binding energy and nonhydrogenic Rydberg series in monolayer WS₂. *Physical review letters* **113**, 076802 (2014).
- 49 Epstein, I. *et al.* Highly confined in-plane propagating exciton-polaritons on monolayer semiconductors. *2D Materials* **7**, 035031 (2020).
- 50 Pettersson, L. A., Roman, L. S. & Inganäs, O. Modeling photocurrent action spectra of photovoltaic devices based on organic thin films. *Journal of Applied Physics* **86**, 487-496 (1999).
- 51 Peumans, P., Yakimov, A. & Forrest, S. R. Small molecular weight organic thin-film photodetectors and solar cells. *Journal of Applied Physics* **93**, 3693-3723 (2003).
- 52 Reshef, O., De Leon, I., Alam, M. Z. & Boyd, R. W. Nonlinear optical effects in epsilon-near-zero media. *Nature Reviews Materials* **4**, 535-551 (2019).
- 53 Liberal, I. & Engheta, N. Zero-index structures as an alternative platform for quantum optics. *Proceedings of the National Academy of Sciences* **114**, 822-827 (2017).
- 54 Ma, E. Y. *et al.* The reststrahlen effect in the optically thin limit: A framework for resonant response in thin media. *Nano Letters* **22**, 8389-8393 (2022).
- 55 Basov, D., Fogler, M. & García de Abajo, F. Polaritons in van der Waals materials. *Science* **354**, aag1992 (2016).
- 56 Jackson, E., Tischler, J., Ratchford, D. & Ellis, C. The role of losses in determining hyperbolic material figures of merit. *Scientific Reports* **14**, 25156 (2024).
- 57 Novotny, L. & Hecht, B. *Principles of nano-optics*. (Cambridge university press, 2012).
- 58 Maier, S. A. *Plasmonics: fundamentals and applications*. Vol. 1 (Springer, 2007).
- 59 Wang, H. *et al.* Strain-Tunable Hyperbolic Exciton Polaritons in Monolayer Black Arsenic with Two Exciton Resonances. *Nano letters* **24**, 2057-2062 (2024).
- 60 Caldwell, J. D. *et al.* Sub-diffractive volume-confined polaritons in the natural hyperbolic material hexagonal boron nitride. *Nature communications* **5**, 5221 (2014).
- 61 Eini, T., Asherov, T., Mazor, Y. & Epstein, I. Valley-polarized hyperbolic exciton polaritons in few-layer two-dimensional semiconductors at visible frequencies. *Physical Review B* **106**, L201405 (2022).
- 62 Low, T. *et al.* Polaritons in layered two-dimensional materials. *Nature materials* **16**, 182-194 (2017).
- 63 Fei, Z. *et al.* Nano-optical imaging of WS₂ waveguide modes revealing light-exciton interactions. *Physical Review B* **94**, 081402 (2016).
- 64 Pizzocchero, F. *et al.* The hot pick-up technique for batch assembly of van der Waals heterostructures. *Nature communications* **7**, 11894 (2016).
- 65 Malitson, I. H. & Dodge, M. J. Refractive index and birefringence of synthetic sapphire. *J. Opt. Soc. Am* **62**, 1405 (1972).
- 66 McPeak, K. M. *et al.* Plasmonic films can easily be better: rules and recipes. *ACS photonics* **2**, 326-333 (2015).

Supporting Information

Natural Hyperbolicity of Hexagonal Boron Nitride in the Deep Ultraviolet

Bongjun Choi¹, Jason Lynch¹, Wangleong Chen², Seong-Joon Jeon³, Hyungseob Cho³, Kyungmin Yang¹, Jonghwan Kim^{3,4,5*}, Nader Engheta^{1,2,6,7*}, Deep Jariwala^{1,2*}

¹Department of Electrical and Systems Engineering, University of Pennsylvania, Philadelphia, Pennsylvania 19104, United States

²Department of Materials Science and Engineering, University of Pennsylvania, Philadelphia, Pennsylvania 19104, United States

³Department of Materials Science and Engineering, Pohang University of Science and Technology, Pohang, Republic of Korea.

⁴Department of Physics, Pohang University of Science and Technology, Pohang, Republic of Korea.

⁵Center for van der Waals Quantum Solids, Institute for Basic Science (IBS), Pohang, Republic of Korea

⁶Department of Bioengineering, University of Pennsylvania, Philadelphia, Pennsylvania 19104, United States

⁷Department of Physics and Astronomy, University of Pennsylvania, Philadelphia, Pennsylvania, 19104, United States

* Corresponding authors: dmj@seas.upenn.edu, engheta@seas.upenn.edu, jonghwankim@postech.ac.kr

The supporting information file includes:

Figure S1. Map data of Ψ and Δ .

Figure S2. Ellipsometry measurement results.

Figure S3. Absorption coefficient of hBN.

Figure S4. Determination of hBN thickness

Figure S5. Simulated absorbance from monolayer hBN.

Figure S6. Comparison of birefringence.

Figure S7. The Reststrahlen band of hBN in the DUV regime.

Figure S8. Isofrequency surface outside of the hyperbolic regime.

Figure S9. Isofrequency surface of the hyperbolic regime.

Figure S10. Simulated partial LDOS and Purcell factor

Figure S11. Simulated electric profile from dipole.

Figure S12. Excitation of high-k mode in the far field.

Figure S13. Simulated electric profile in hyperbolic regime.

Figure S14. Propagation distance of HEP.

Note 1. Analysis of imaging spectroscopic ellipsometry data

Table 1. Anisotropic, complex refractive index of hBN

References

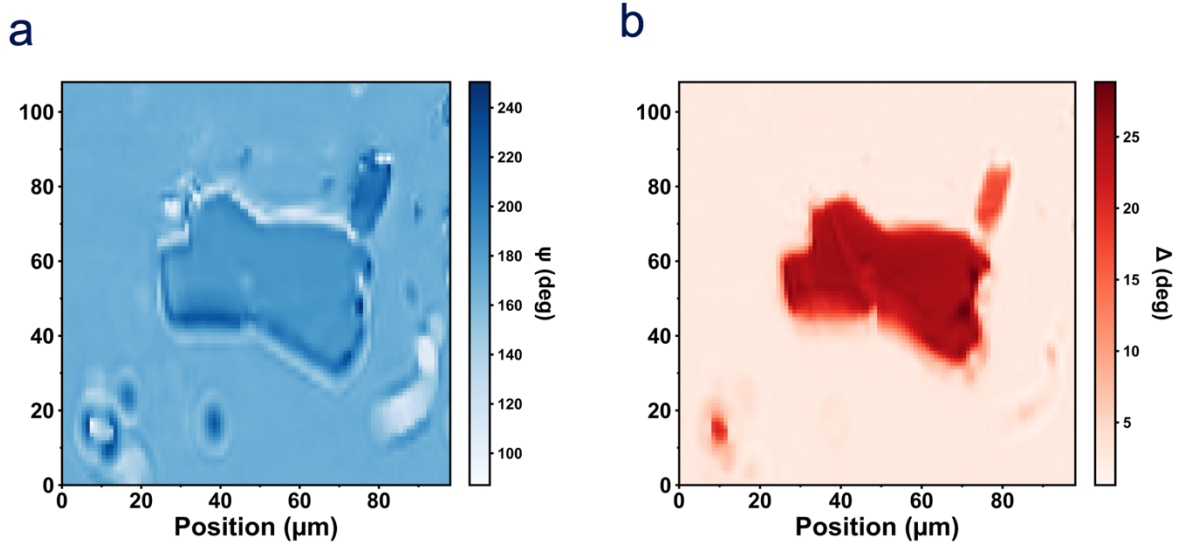


Figure S1. Two-dimensional (2D) map data at 250 nm of (a) Ψ (the amplitude ratio) and (b) Δ (the phase difference) value from hBN using imaging spectroscopic ellipsometry (ISE). ISE allows simultaneous measurement of all pixels inside the area of interest (AOI). Each pixel $\sim 1 \times 1 \mu\text{m}$ contains the Ψ and Δ information.

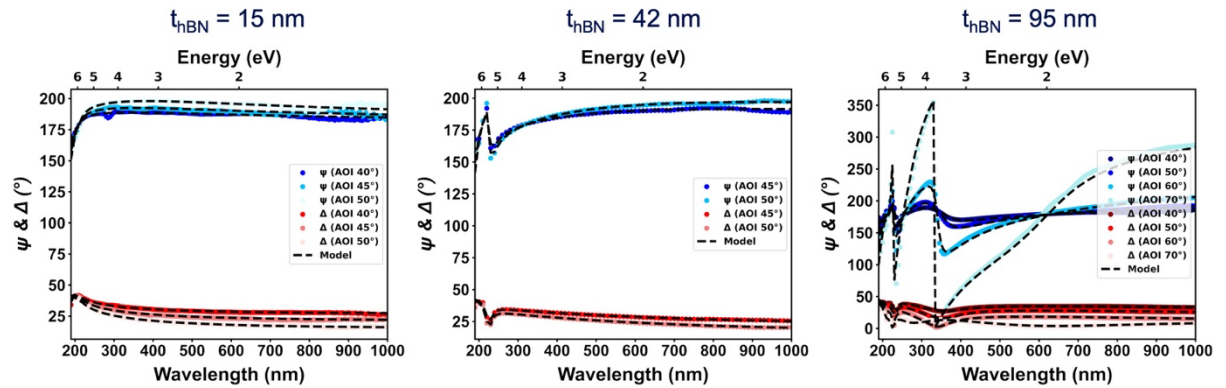


Figure S2. Measured Ψ and Δ values for hBN films with varying thicknesses (15, 42, and 95 nm) and incident angles ($40^\circ \sim 70^\circ$), overlaid with fitted curves based on a multi-Lorentz oscillator model. hBN was treated as a uniaxial material with independently fitted in-plane and out-of-plane components¹, demonstrating high fidelity of the optical model.

Note S1. Analysis of imaging spectroscopic ellipsometry data

In ellipsometry measurement, the p- (transverse magnetic (TM)) and s- (transverse electric (TE)) polarized light are incident on the sample, measuring the polarization state of reflected light. Once the p- and s-polarizations of light hit the sample, each polarization of light shows different changes in amplitude and phase, and ellipsometry measures two parameters, Ψ and Δ , which represent the difference of amplitude and phase given by Eq. (1), where r_p and r_s are the Fresnel coefficients¹.

$$\rho = \frac{r_p}{r_s} = \tan \psi \exp(i\Delta) \quad (1)$$

Ellipsometry is a model-based technique that requires two models to analyze the measured ISE data: the geometric structure of the sample and the dielectric function model. The geometric structure refers to the stacking sequence of the sample, including layer thicknesses. In order to increase the signal to noise ratio (SNR) in the DUV regime, we choose Al_2O_3 as a substrate due to its wide bandgap, and transferred the exfoliated hBN crystals. Thus, geometric structure is defined as an air / hBN (t nm) / Al_2O_3 (Substrate). Dielectric function model can describe the optical response, and especially electron transitions and exciton resonances are widely modelled using Lorentz oscillator model given by Eq. (2), where the resonance energy is E_0 , f is the oscillator strength, and a damping factor is Γ .

$$\varepsilon_{\text{Lorentz}}(E) = \frac{f E_0 \Gamma}{E_0^2 - E^2 - i\Gamma E} \quad (2)$$

If there are multiple oscillators in the systems, the system can be described by the sum of Lorentz oscillator model described in Eq. (3), where ε_∞ is a background permittivity accounting for high-energy electronic transitions that lie outside the measurable spectral range.

$$\varepsilon(E) = \varepsilon_\infty + \sum_i \varepsilon_{\text{Lorentz}}^i(E) \quad (3)$$

Since hBN has an anisotropy along z axis (uniaxial material), the dielectric tensor of hBN is represented by Eq. (4) since $\varepsilon_{xx} = \varepsilon_{yy}$.

$$\varepsilon = \begin{bmatrix} \varepsilon_{xx} & 0 & 0 \\ 0 & \varepsilon_{xx} & 0 \\ 0 & 0 & \varepsilon_{zz} \end{bmatrix} \quad (4)$$

Thus, ε_{xx} (in-plane permittivity) and ε_{zz} (out-of-plane permittivity) should be modelled respectively. Following previous literature²⁻⁴, we model both in-plane and out-of-plane permittivity using multiple Lorentz oscillators within a uniaxial dielectric model, which accurately reproduces the experimental data, as shown in Fig. S2.

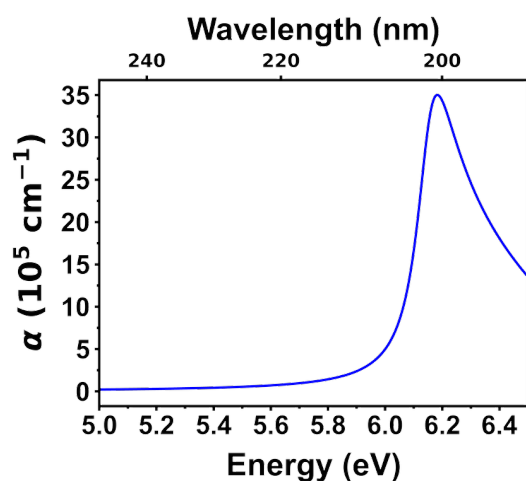


Figure S3. Absorption coefficient ($\alpha = 4\pi k/\lambda$) of hBN as a function of photon energy (wavelength), showing significant absorption coefficient due to the strong exciton oscillator strength.

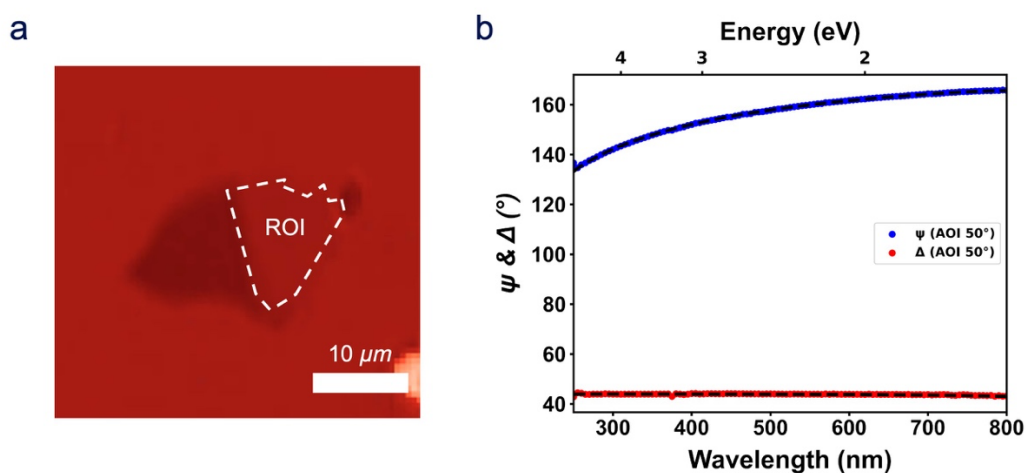


Figure S4. Determination of hBN thickness using imaging spectroscopic ellipsometry (ISE). (a) Mapped Δ values from thin hBN. (b) Fitted curves based on hBN refractive indices, indicating a hBN thickness of $\sim 1.67 \text{ nm}$ (5 layers).

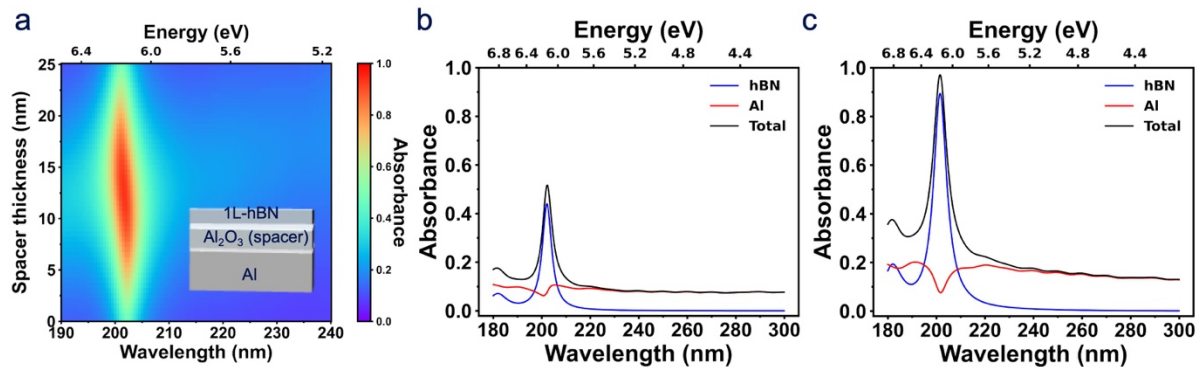


Figure S5. (a) Simulated absorbance spectrum using transfer matrix method (TMM)⁵⁻⁷ calculation in a 1L-hBN/Al₂O₃/Al heterostructure as a function of Al₂O₃ spacer thickness, demonstrating the high absorbance from only a monolayer hBN layer due to strong exciton resonance. Note that we assume that monolayer hBN has the same refractive index as that of bulk for the calculation. Layer resolved absorbance spectrum depending on the presence and absence of the spacer structure: (b) 1L-hBN/Al (100 nm) and (c) 1L-hBN/Al₂O₃ (13.5 nm) /Al (100 nm). Even a monolayer of hBN on the Al substrate can absorb a significant amount of light. In addition, once an appropriate thickness of Al₂O₃ is added, absorbance can reach approximately unity absorption from a monolayer of hBN. Layer resolved absorbance calculation shows that this significant amount of absorption mostly comes from the hBN monolayer for both (b) and (c) structures, indicating the strong exciton strength in hBN.

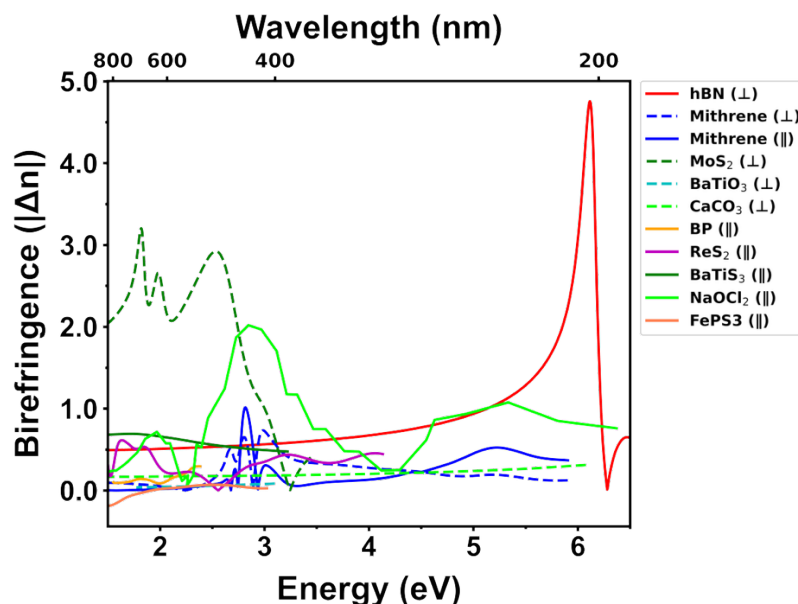


Figure S6. Comparison of the in-plane and out-of-plane birefringence magnitude as a function of wavelength for various birefringent crystals⁸⁻¹⁶, including hBN. hBN exhibits exceptionally large birefringence spanning the visible to the deep ultraviolet (DUV) range. Notably, it shows significant birefringence in the DUV regime, surpassing recently reported NaOCl₂, an uncommon and remarkable property.

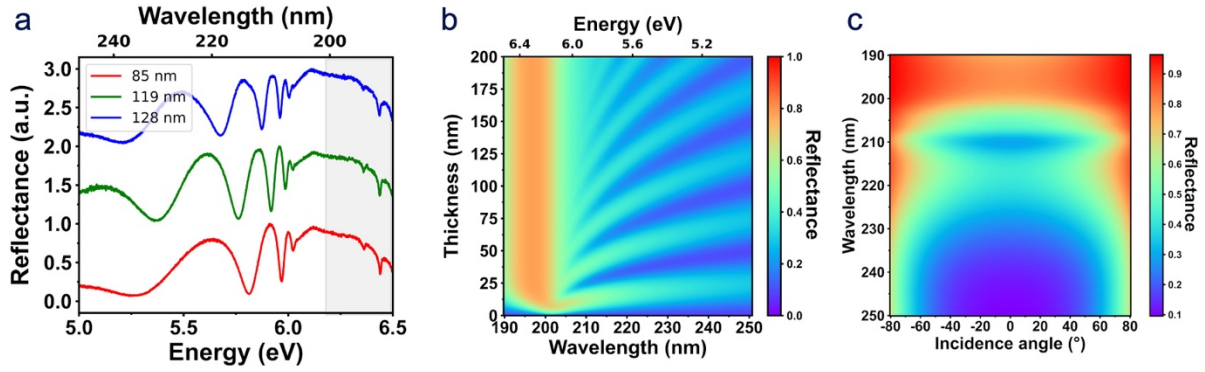


Figure S7. (a) The measured reflectance spectrum with hBN on Al_2O_3 substrate reveals the Reststrahlen band (grey-shaded region), exhibiting high reflectance across multiple hBN thicknesses. Simulated reflectance spectrum using TMM as a function of wavelength /thickness/incidence angle, showing the Reststrahlen band of hBN in the DUV regime in good agreement with experimental results in (a). (b) The thickness of hBN was changed on the Al_2O_3 substrate. As the hBN thickness approaches the optically thin limit, the Reststrahlen band changes to a single resonance. On the other hand, the thick enough hBN (> 25 nm), which is in the strong response regime, shows high reflectance. (c) Calculated reflectance as a function of the incidence angle of hBN (50nm) on the Al_2O_3 substrate structure, indicating a highly reflective nature of the Reststrahlen band in a wide range of incidence angles.

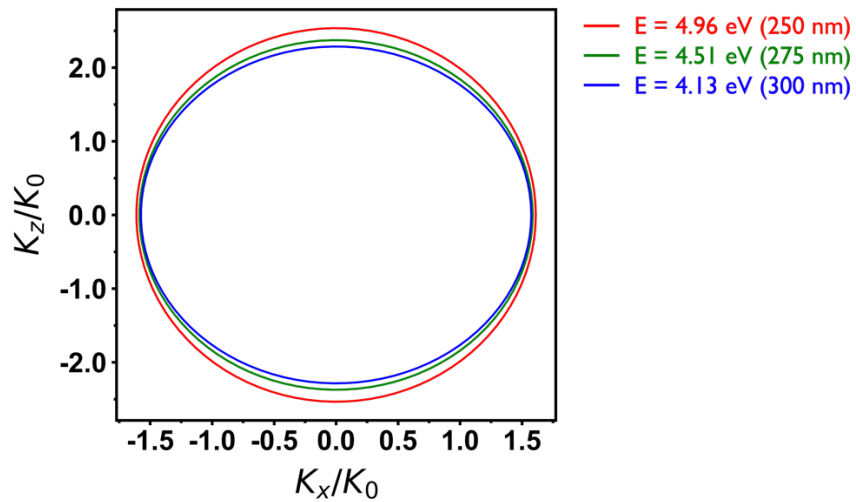


Figure S8. Isofrequency surface in various photon energies (wavelengths) of hBN outside of the hyperbolic regime, showing the elliptical dispersion.

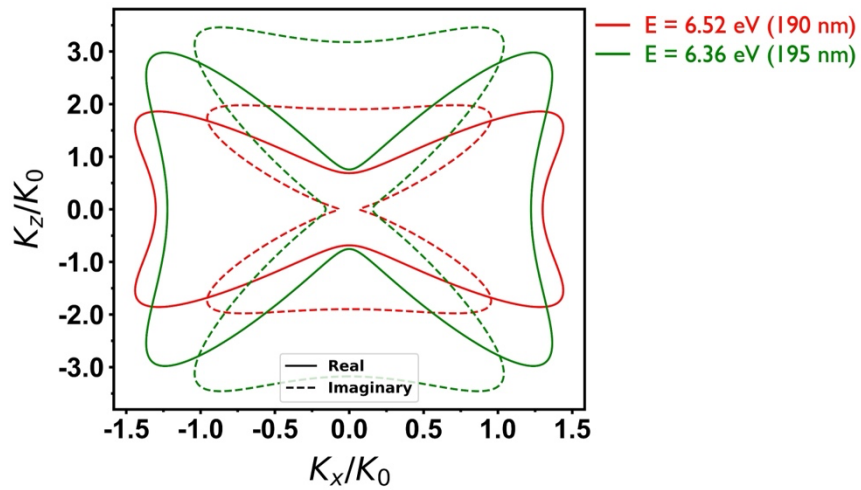


Figure S9. Isofrequency surface in various photon energies (wavelengths) of hBN in the hyperbolic regime, showing the hyperbolic dispersion.

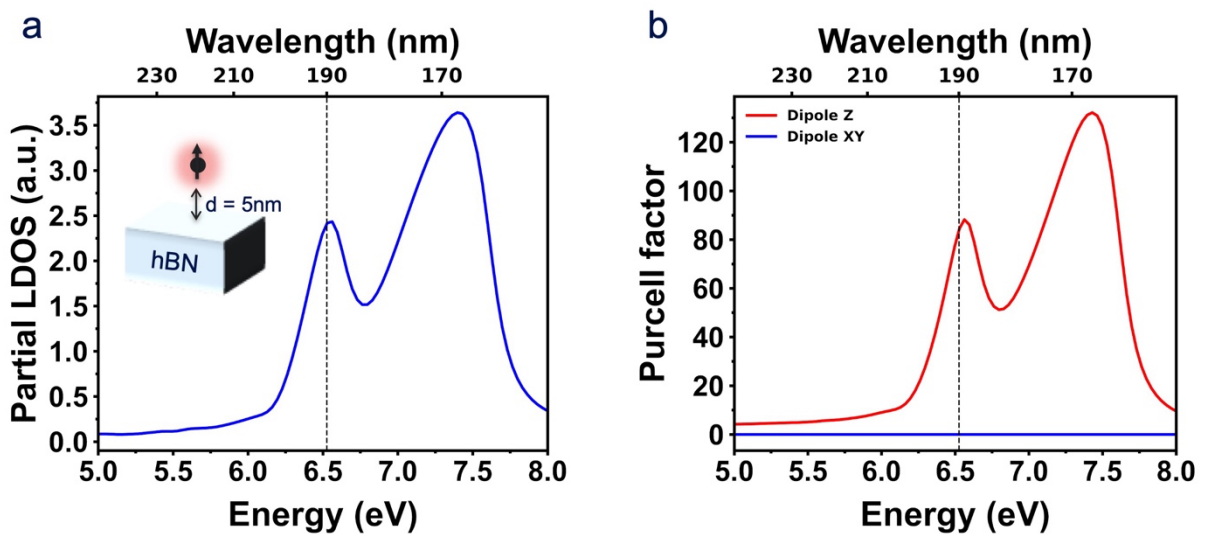


Figure S10. (a) Calculated partial local density of states (LDOS) using finite-difference time-domain (FDTD) simulations. The dipole along the z-axis is located 5 nm above the hBN, as illustrated in the inset. The partial LDOS can be calculated from the imaginary part of the Green's function, demonstrating the larger partial LDOS in the hyperbolic regime¹⁷. (b) Simulated Purcell factor depending on the dipole orientation under the same conditions in (a). When the dipole is oriented along the z direction, the significant Purcell factor can be achieved, consistent with the partial LDOS calculation, as the Purcell factor is proportional to the LDOS. In contrast, an in-plane-oriented dipole does not contribute to emission enhancement, highlighting the critical role of hyperbolic dispersion in boosting the Purcell factor in hBN. In addition, a notable Purcell factor can be achieved around the epsilon near-zero (ENZ) point^{18,19}.

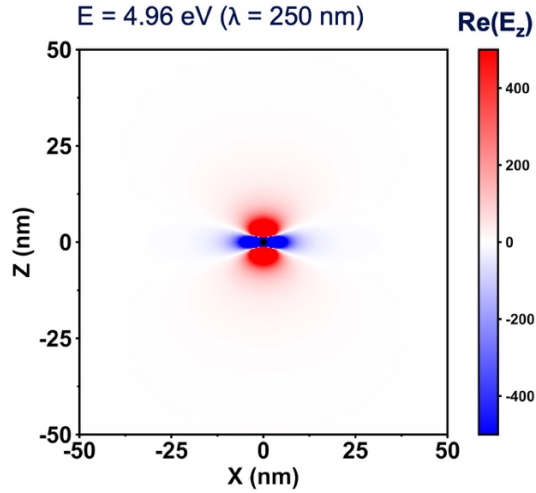


Figure S11. Numerically simulated near-field distribution obtained from FDTD simulations shows the wave launched by a point dipole oriented along the Z-axis, outside the hyperbolic regime, in the XZ plane, exhibiting non-directional propagation behavior.

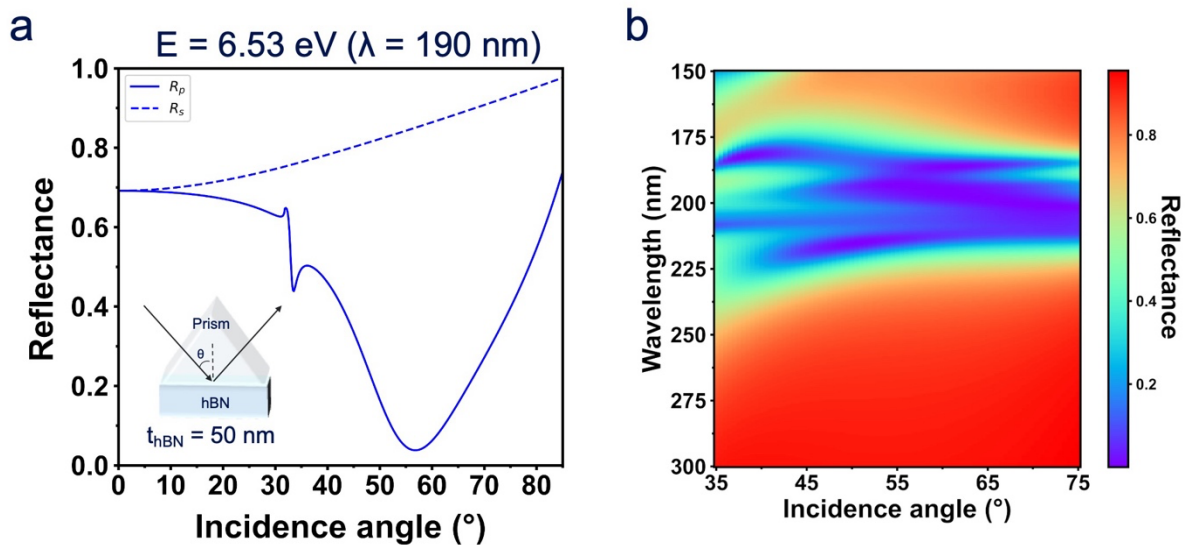


Figure S12. (a) The calculated reflectance spectrum of 50 nm of hBN as a function of incidence angle at $E = 6.53$ eV ($\lambda = 190$ nm), depending on the polarization of incidence light (s (TE) and p (TM) polarization). Otto configuration is adapted using a high-index prism (Al_2O_3) to launch the highly confined high-k mode²⁰. TE polarized light shows high reflectance due to the existence of Reststrahlen in hBN. In contrast, the pronounced dip appears around a 30° incidence angle in the TM polarized light incidence due to the coupling with the high-k mode²⁰. Furthermore, Brewster's angle is observed around a 60° incidence angle, consistent with theoretical predictions calculated from the dielectric constants of the media. (b) The simulated reflectance spectrum as a function of incidence angle and wavelength, indicating a clear high-k wave launch in the hyperbolic window.

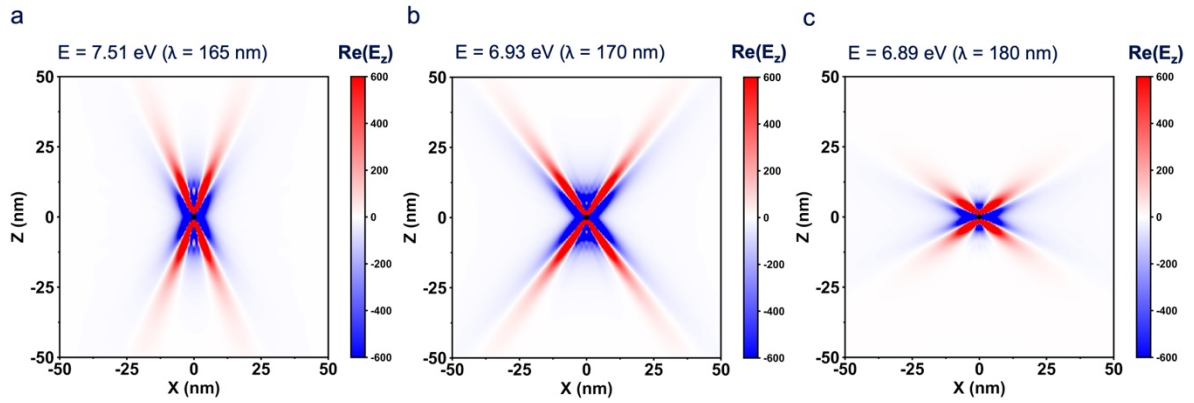


Figure S13. Numerically simulated near-field wave propagation obtained from FDTD simulations as a function of photon energies (wavelengths) (a) 7.51 eV ($\lambda = 165$ nm), (b) 6.93 eV ($\lambda = 170$ nm), and (c) 6.89 eV ($\lambda = 180$ nm), showing highly directional propagation depending on the photon energies (wavelengths) in hyperbolic regime.

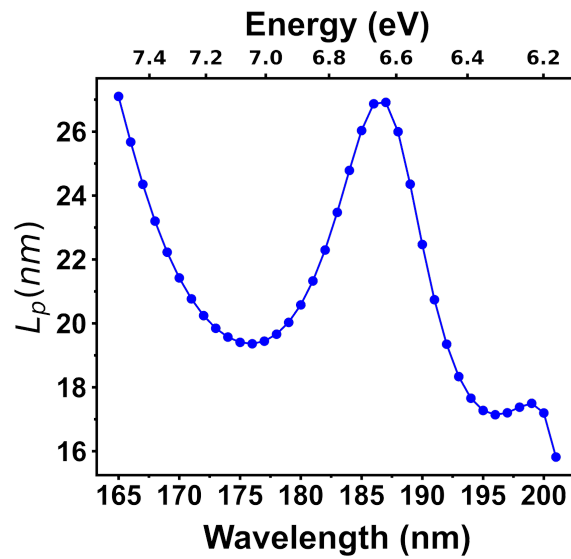


Figure S14. The propagation length of hyperbolic exciton polaritons (HEP) along the direction corresponding to the maximum real part of the wavevector in the hyperbolic regime²¹.

Table 1. Anisotropic, complex refractive index of hBN

wavelength (nm)	$n_{\text{in-plane}} (n_o)$	$k_{\text{in-plane}} (k_o)$	$n_{\text{out-of-plane}} (n_e)$	$k_{\text{out-of-plane}} (k_e)$
190	0.6866	1.8992	1.3006	0.0704
191	0.6398	2.1088	1.2873	0.0814
192	0.6234	2.3385	1.2728	0.0948
193	0.6355	2.5894	1.2571	0.1114
194	0.6774	2.8663	1.2403	0.1321
195	0.7552	3.1769	1.2229	0.1582
196	0.882	3.5321	1.2057	0.1912
197	1.0838	3.9453	1.1904	0.233
198	1.4114	4.429	1.1801	0.2854
199	1.9646	4.9751	1.1797	0.3494
200	2.9206	5.4731	1.196	0.4237
201	4.3979	5.4884	1.2363	0.5027
202	5.7732	4.4482	1.3058	0.5758
203	6.1308	2.9839	1.4032	0.6285
204	5.8395	1.9483	1.5183	0.6467
205	5.4229	1.3385	1.6326	0.6244
206	5.0454	0.9747	1.7269	0.5681
207	4.7314	0.745	1.7908	0.4935
208	4.4735	0.5916	1.8255	0.4165
209	4.2602	0.484	1.838	0.3469
210	4.0815	0.4055	1.8366	0.2882
211	3.9298	0.3463	1.8273	0.2405
212	3.7996	0.3005	1.8141	0.2022
213	3.6865	0.2642	1.7994	0.1716
214	3.5873	0.2349	1.7846	0.1471
215	3.4996	0.2108	1.7702	0.1272
216	3.4214	0.1907	1.7567	0.111
217	3.3512	0.1738	1.7441	0.0976
218	3.2879	0.1593	1.7325	0.0866
219	3.2303	0.1469	1.7219	0.0773
220	3.1779	0.1361	1.7121	0.0694
221	3.1298	0.1266	1.7031	0.0627
222	3.0855	0.1183	1.6949	0.0569
223	3.0447	0.1109	1.6873	0.052
224	3.0068	0.1043	1.6803	0.0476
225	2.9716	0.0984	1.6738	0.0438
226	2.9388	0.0931	1.6678	0.0405
227	2.9081	0.0883	1.6623	0.0376
228	2.8794	0.0839	1.6571	0.0349

229	2.8524	0.08	1.6523	0.0326
230	2.827	0.0763	1.6478	0.0305
231	2.8031	0.073	1.6436	0.0286
232	2.7805	0.0699	1.6397	0.0269
233	2.7591	0.067	1.636	0.0253
234	2.7389	0.0644	1.6326	0.0239
235	2.7196	0.062	1.6293	0.0226
236	2.7013	0.0597	1.6263	0.0215
237	2.6839	0.0576	1.6234	0.0204
238	2.6674	0.0556	1.6206	0.0194
239	2.6515	0.0537	1.618	0.0185
240	2.6364	0.052	1.6156	0.0176
241	2.622	0.0504	1.6133	0.0168
242	2.6081	0.0488	1.611	0.0161
243	2.5949	0.0474	1.6089	0.0154
244	2.5822	0.046	1.6069	0.0148
245	2.5699	0.0447	1.605	0.0142
246	2.5582	0.0435	1.6032	0.0137
247	2.5469	0.0423	1.6014	0.0131
248	2.5361	0.0412	1.5997	0.0127
249	2.5256	0.0402	1.5981	0.0122
250	2.5155	0.0392	1.5966	0.0118
251	2.5058	0.0383	1.5951	0.0114
252	2.4964	0.0374	1.5937	0.011
253	2.4874	0.0365	1.5924	0.0106
254	2.4786	0.0357	1.5911	0.0103
255	2.4702	0.0349	1.5898	0.01
256	2.462	0.0341	1.5886	0.0097
257	2.454	0.0334	1.5875	0.0094
258	2.4464	0.0327	1.5863	0.0091
259	2.4389	0.0321	1.5853	0.0088
260	2.4317	0.0314	1.5842	0.0086
261	2.4247	0.0308	1.5832	0.0084
262	2.4179	0.0302	1.5822	0.0081
263	2.4113	0.0297	1.5813	0.0079
264	2.4049	0.0291	1.5804	0.0077
265	2.3987	0.0286	1.5795	0.0075
266	2.3926	0.0281	1.5787	0.0073
267	2.3867	0.0276	1.5778	0.0072
268	2.381	0.0272	1.577	0.007
269	2.3754	0.0267	1.5763	0.0068
270	2.37	0.0263	1.5755	0.0067

271	2.3647	0.0259	1.5748	0.0065
272	2.3596	0.0254	1.5741	0.0064
273	2.3546	0.025	1.5734	0.0062
274	2.3497	0.0247	1.5727	0.0061
275	2.3449	0.0243	1.5721	0.006
276	2.3403	0.0239	1.5714	0.0058
277	2.3357	0.0236	1.5708	0.0057
278	2.3313	0.0233	1.5702	0.0056
279	2.3269	0.0229	1.5696	0.0055
280	2.3227	0.0226	1.5691	0.0054
281	2.3186	0.0223	1.5685	0.0053
282	2.3146	0.022	1.568	0.0052
283	2.3106	0.0217	1.5675	0.0051
284	2.3068	0.0214	1.567	0.005
285	2.303	0.0211	1.5665	0.0049
286	2.2993	0.0209	1.566	0.0048
287	2.2957	0.0206	1.5655	0.0047
288	2.2921	0.0204	1.565	0.0047
289	2.2887	0.0201	1.5646	0.0046
290	2.2853	0.0199	1.5641	0.0045
291	2.282	0.0196	1.5637	0.0044
292	2.2787	0.0194	1.5633	0.0043
293	2.2756	0.0192	1.5629	0.0043
294	2.2724	0.019	1.5625	0.0042
295	2.2694	0.0188	1.5621	0.0041
296	2.2664	0.0186	1.5617	0.0041
297	2.2635	0.0183	1.5613	0.004
298	2.2606	0.0181	1.561	0.004
299	2.2578	0.018	1.5606	0.0039
300	2.255	0.0178	1.5602	0.0038
301	2.2523	0.0176	1.5599	0.0038
302	2.2496	0.0174	1.5596	0.0037
303	2.247	0.0172	1.5592	0.0037
304	2.2444	0.0171	1.5589	0.0036
305	2.2419	0.0169	1.5586	0.0036
306	2.2394	0.0167	1.5583	0.0035
307	2.237	0.0166	1.558	0.0035
308	2.2346	0.0164	1.5577	0.0034
309	2.2322	0.0162	1.5574	0.0034
310	2.2299	0.0161	1.5571	0.0033
311	2.2277	0.0159	1.5568	0.0033
312	2.2254	0.0158	1.5565	0.0033

313	2.2232	0.0157	1.5563	0.0032
314	2.2211	0.0155	1.556	0.0032
315	2.219	0.0154	1.5557	0.0031
316	2.2169	0.0152	1.5555	0.0031
317	2.2148	0.0151	1.5552	0.0031
318	2.2128	0.015	1.555	0.003
319	2.2108	0.0148	1.5547	0.003
320	2.2089	0.0147	1.5545	0.003
321	2.207	0.0146	1.5543	0.0029
322	2.2051	0.0145	1.554	0.0029
323	2.2032	0.0144	1.5538	0.0029
324	2.2014	0.0142	1.5536	0.0028
325	2.1996	0.0141	1.5534	0.0028
326	2.1978	0.014	1.5532	0.0028
327	2.1961	0.0139	1.5529	0.0027
328	2.1944	0.0138	1.5527	0.0027
329	2.1927	0.0137	1.5525	0.0027
330	2.191	0.0136	1.5523	0.0026
331	2.1894	0.0135	1.5521	0.0026
332	2.1877	0.0134	1.5519	0.0026
333	2.1861	0.0133	1.5517	0.0026
334	2.1846	0.0132	1.5516	0.0025
335	2.183	0.0131	1.5514	0.0025
336	2.1815	0.013	1.5512	0.0025
337	2.18	0.0129	1.551	0.0025
338	2.1785	0.0128	1.5508	0.0024
339	2.1771	0.0127	1.5507	0.0024
340	2.1756	0.0126	1.5505	0.0024
341	2.1742	0.0125	1.5503	0.0024
342	2.1728	0.0125	1.5502	0.0024
343	2.1714	0.0124	1.55	0.0023
344	2.17	0.0123	1.5498	0.0023
345	2.1687	0.0122	1.5497	0.0023
346	2.1674	0.0121	1.5495	0.0023
347	2.1661	0.012	1.5494	0.0022
348	2.1648	0.012	1.5492	0.0022
349	2.1635	0.0119	1.5491	0.0022
350	2.1622	0.0118	1.5489	0.0022
351	2.161	0.0117	1.5488	0.0022
352	2.1598	0.0117	1.5486	0.0022
353	2.1586	0.0116	1.5485	0.0021
354	2.1574	0.0115	1.5483	0.0021

355	2.1562	0.0115	1.5482	0.0021
356	2.155	0.0114	1.5481	0.0021
357	2.1539	0.0113	1.5479	0.0021
358	2.1528	0.0112	1.5478	0.002
359	2.1516	0.0112	1.5477	0.002
360	2.1505	0.0111	1.5475	0.002
361	2.1495	0.011	1.5474	0.002
362	2.1484	0.011	1.5473	0.002
363	2.1473	0.0109	1.5472	0.002
364	2.1463	0.0109	1.547	0.002
365	2.1452	0.0108	1.5469	0.0019
366	2.1442	0.0107	1.5468	0.0019
367	2.1432	0.0107	1.5467	0.0019
368	2.1422	0.0106	1.5466	0.0019
369	2.1412	0.0105	1.5465	0.0019
370	2.1402	0.0105	1.5463	0.0019
371	2.1393	0.0104	1.5462	0.0019
372	2.1383	0.0104	1.5461	0.0018
373	2.1374	0.0103	1.546	0.0018
374	2.1364	0.0103	1.5459	0.0018
375	2.1355	0.0102	1.5458	0.0018
376	2.1346	0.0102	1.5457	0.0018
377	2.1337	0.0101	1.5456	0.0018
378	2.1328	0.01	1.5455	0.0018
379	2.1319	0.01	1.5454	0.0017
380	2.131	0.0099	1.5453	0.0017
381	2.1302	0.0099	1.5452	0.0017
382	2.1293	0.0098	1.5451	0.0017
383	2.1285	0.0098	1.545	0.0017
384	2.1277	0.0097	1.5449	0.0017
385	2.1268	0.0097	1.5448	0.0017
386	2.126	0.0096	1.5447	0.0017
387	2.1252	0.0096	1.5446	0.0017
388	2.1244	0.0095	1.5445	0.0016
389	2.1236	0.0095	1.5444	0.0016
390	2.1229	0.0095	1.5444	0.0016
391	2.1221	0.0094	1.5443	0.0016
392	2.1213	0.0094	1.5442	0.0016
393	2.1206	0.0093	1.5441	0.0016
394	2.1198	0.0093	1.544	0.0016
395	2.1191	0.0092	1.5439	0.0016
396	2.1184	0.0092	1.5439	0.0016

397	2.1176	0.0091	1.5438	0.0016
398	2.1169	0.0091	1.5437	0.0015
399	2.1162	0.0091	1.5436	0.0015
400	2.1155	0.009	1.5435	0.0015
401	2.1148	0.009	1.5435	0.0015
402	2.1141	0.0089	1.5434	0.0015
403	2.1134	0.0089	1.5433	0.0015
404	2.1128	0.0089	1.5432	0.0015
405	2.1121	0.0088	1.5431	0.0015
406	2.1114	0.0088	1.5431	0.0015
407	2.1108	0.0087	1.543	0.0015
408	2.1101	0.0087	1.5429	0.0015
409	2.1095	0.0087	1.5429	0.0014
410	2.1089	0.0086	1.5428	0.0014
411	2.1082	0.0086	1.5427	0.0014
412	2.1076	0.0086	1.5426	0.0014
413	2.107	0.0085	1.5426	0.0014
414	2.1064	0.0085	1.5425	0.0014
415	2.1058	0.0084	1.5424	0.0014
416	2.1052	0.0084	1.5424	0.0014
417	2.1046	0.0084	1.5423	0.0014
418	2.104	0.0083	1.5422	0.0014
419	2.1034	0.0083	1.5422	0.0014
420	2.1029	0.0083	1.5421	0.0014
421	2.1023	0.0082	1.5421	0.0014
422	2.1017	0.0082	1.542	0.0014
423	2.1012	0.0082	1.5419	0.0013
424	2.1006	0.0081	1.5419	0.0013
425	2.1001	0.0081	1.5418	0.0013
426	2.0995	0.0081	1.5417	0.0013
427	2.099	0.008	1.5417	0.0013
428	2.0985	0.008	1.5416	0.0013
429	2.0979	0.008	1.5416	0.0013
430	2.0974	0.0079	1.5415	0.0013
431	2.0969	0.0079	1.5415	0.0013
432	2.0964	0.0079	1.5414	0.0013
433	2.0959	0.0079	1.5413	0.0013
434	2.0954	0.0078	1.5413	0.0013
435	2.0949	0.0078	1.5412	0.0013
436	2.0944	0.0078	1.5412	0.0013
437	2.0939	0.0077	1.5411	0.0013
438	2.0934	0.0077	1.5411	0.0012

439	2.0929	0.0077	1.541	0.0012
440	2.0924	0.0076	1.541	0.0012
441	2.0919	0.0076	1.5409	0.0012
442	2.0915	0.0076	1.5409	0.0012
443	2.091	0.0076	1.5408	0.0012
444	2.0905	0.0075	1.5408	0.0012
445	2.0901	0.0075	1.5407	0.0012
446	2.0896	0.0075	1.5407	0.0012
447	2.0892	0.0075	1.5406	0.0012
448	2.0887	0.0074	1.5406	0.0012
449	2.0883	0.0074	1.5405	0.0012
450	2.0878	0.0074	1.5405	0.0012
451	2.0874	0.0073	1.5404	0.0012
452	2.087	0.0073	1.5404	0.0012
453	2.0866	0.0073	1.5403	0.0012
454	2.0861	0.0073	1.5403	0.0012
455	2.0857	0.0072	1.5402	0.0012
456	2.0853	0.0072	1.5402	0.0011
457	2.0849	0.0072	1.5401	0.0011
458	2.0845	0.0072	1.5401	0.0011
459	2.0841	0.0071	1.54	0.0011
460	2.0837	0.0071	1.54	0.0011
461	2.0833	0.0071	1.54	0.0011
462	2.0829	0.0071	1.5399	0.0011
463	2.0825	0.007	1.5399	0.0011
464	2.0821	0.007	1.5398	0.0011
465	2.0817	0.007	1.5398	0.0011
466	2.0813	0.007	1.5397	0.0011
467	2.0809	0.007	1.5397	0.0011
468	2.0805	0.0069	1.5397	0.0011
469	2.0802	0.0069	1.5396	0.0011
470	2.0798	0.0069	1.5396	0.0011
471	2.0794	0.0069	1.5395	0.0011
472	2.0791	0.0068	1.5395	0.0011
473	2.0787	0.0068	1.5395	0.0011
474	2.0783	0.0068	1.5394	0.0011
475	2.078	0.0068	1.5394	0.0011
476	2.0776	0.0068	1.5393	0.0011
477	2.0773	0.0067	1.5393	0.0011
478	2.0769	0.0067	1.5393	0.001
479	2.0766	0.0067	1.5392	0.001
480	2.0762	0.0067	1.5392	0.001

481	2.0759	0.0066	1.5392	0.001
482	2.0755	0.0066	1.5391	0.001
483	2.0752	0.0066	1.5391	0.001
484	2.0749	0.0066	1.5391	0.001
485	2.0745	0.0066	1.539	0.001
486	2.0742	0.0065	1.539	0.001
487	2.0739	0.0065	1.5389	0.001
488	2.0736	0.0065	1.5389	0.001
489	2.0732	0.0065	1.5389	0.001
490	2.0729	0.0065	1.5388	0.001
491	2.0726	0.0064	1.5388	0.001
492	2.0723	0.0064	1.5388	0.001
493	2.072	0.0064	1.5387	0.001
494	2.0717	0.0064	1.5387	0.001
495	2.0714	0.0064	1.5387	0.001
496	2.0711	0.0063	1.5386	0.001
497	2.0708	0.0063	1.5386	0.001
498	2.0705	0.0063	1.5386	0.001
499	2.0702	0.0063	1.5385	0.001
500	2.0699	0.0063	1.5385	0.001
501	2.0696	0.0063	1.5385	0.001
502	2.0693	0.0062	1.5384	0.001
503	2.069	0.0062	1.5384	0.001
504	2.0687	0.0062	1.5384	0.001
505	2.0684	0.0062	1.5384	0.0009
506	2.0681	0.0062	1.5383	0.0009
507	2.0678	0.0061	1.5383	0.0009
508	2.0676	0.0061	1.5383	0.0009
509	2.0673	0.0061	1.5382	0.0009
510	2.067	0.0061	1.5382	0.0009
511	2.0667	0.0061	1.5382	0.0009
512	2.0665	0.0061	1.5381	0.0009
513	2.0662	0.006	1.5381	0.0009
514	2.0659	0.006	1.5381	0.0009
515	2.0657	0.006	1.5381	0.0009
516	2.0654	0.006	1.538	0.0009
517	2.0651	0.006	1.538	0.0009
518	2.0649	0.006	1.538	0.0009
519	2.0646	0.0059	1.5379	0.0009
520	2.0644	0.0059	1.5379	0.0009
521	2.0641	0.0059	1.5379	0.0009
522	2.0638	0.0059	1.5379	0.0009

523	2.0636	0.0059	1.5378	0.0009
524	2.0633	0.0059	1.5378	0.0009
525	2.0631	0.0059	1.5378	0.0009
526	2.0629	0.0058	1.5378	0.0009
527	2.0626	0.0058	1.5377	0.0009
528	2.0624	0.0058	1.5377	0.0009
529	2.0621	0.0058	1.5377	0.0009
530	2.0619	0.0058	1.5377	0.0009
531	2.0616	0.0058	1.5376	0.0009
532	2.0614	0.0057	1.5376	0.0009
533	2.0612	0.0057	1.5376	0.0009
534	2.0609	0.0057	1.5376	0.0009
535	2.0607	0.0057	1.5375	0.0009
536	2.0605	0.0057	1.5375	0.0009
537	2.0602	0.0057	1.5375	0.0009
538	2.06	0.0057	1.5375	0.0008
539	2.0598	0.0056	1.5374	0.0008
540	2.0596	0.0056	1.5374	0.0008
541	2.0593	0.0056	1.5374	0.0008
542	2.0591	0.0056	1.5374	0.0008
543	2.0589	0.0056	1.5373	0.0008
544	2.0587	0.0056	1.5373	0.0008
545	2.0585	0.0056	1.5373	0.0008
546	2.0582	0.0055	1.5373	0.0008
547	2.058	0.0055	1.5372	0.0008
548	2.0578	0.0055	1.5372	0.0008
549	2.0576	0.0055	1.5372	0.0008
550	2.0574	0.0055	1.5372	0.0008
551	2.0572	0.0055	1.5372	0.0008
552	2.057	0.0055	1.5371	0.0008
553	2.0568	0.0054	1.5371	0.0008
554	2.0566	0.0054	1.5371	0.0008
555	2.0564	0.0054	1.5371	0.0008
556	2.0562	0.0054	1.537	0.0008
557	2.056	0.0054	1.537	0.0008
558	2.0558	0.0054	1.537	0.0008
559	2.0556	0.0054	1.537	0.0008
560	2.0554	0.0054	1.537	0.0008
561	2.0552	0.0053	1.5369	0.0008
562	2.055	0.0053	1.5369	0.0008
563	2.0548	0.0053	1.5369	0.0008
564	2.0546	0.0053	1.5369	0.0008

565	2.0544	0.0053	1.5369	0.0008
566	2.0542	0.0053	1.5368	0.0008
567	2.054	0.0053	1.5368	0.0008
568	2.0538	0.0053	1.5368	0.0008
569	2.0536	0.0052	1.5368	0.0008
570	2.0534	0.0052	1.5368	0.0008
571	2.0533	0.0052	1.5367	0.0008
572	2.0531	0.0052	1.5367	0.0008
573	2.0529	0.0052	1.5367	0.0008
574	2.0527	0.0052	1.5367	0.0008
575	2.0525	0.0052	1.5367	0.0008
576	2.0524	0.0052	1.5366	0.0008
577	2.0522	0.0051	1.5366	0.0008
578	2.052	0.0051	1.5366	0.0008
579	2.0518	0.0051	1.5366	0.0008
580	2.0516	0.0051	1.5366	0.0008
581	2.0515	0.0051	1.5366	0.0008
582	2.0513	0.0051	1.5365	0.0007
583	2.0511	0.0051	1.5365	0.0007
584	2.051	0.0051	1.5365	0.0007
585	2.0508	0.005	1.5365	0.0007
586	2.0506	0.005	1.5365	0.0007
587	2.0505	0.005	1.5364	0.0007
588	2.0503	0.005	1.5364	0.0007
589	2.0501	0.005	1.5364	0.0007
590	2.05	0.005	1.5364	0.0007
591	2.0498	0.005	1.5364	0.0007
592	2.0496	0.005	1.5364	0.0007
593	2.0495	0.005	1.5363	0.0007
594	2.0493	0.0049	1.5363	0.0007
595	2.0491	0.0049	1.5363	0.0007
596	2.049	0.0049	1.5363	0.0007
597	2.0488	0.0049	1.5363	0.0007
598	2.0487	0.0049	1.5363	0.0007
599	2.0485	0.0049	1.5362	0.0007
600	2.0484	0.0049	1.5362	0.0007
601	2.0482	0.0049	1.5362	0.0007
602	2.048	0.0049	1.5362	0.0007
603	2.0479	0.0049	1.5362	0.0007
604	2.0477	0.0048	1.5362	0.0007
605	2.0476	0.0048	1.5361	0.0007
606	2.0474	0.0048	1.5361	0.0007

607	2.0473	0.0048	1.5361	0.0007
608	2.0471	0.0048	1.5361	0.0007
609	2.047	0.0048	1.5361	0.0007
610	2.0468	0.0048	1.5361	0.0007
611	2.0467	0.0048	1.536	0.0007
612	2.0466	0.0048	1.536	0.0007
613	2.0464	0.0048	1.536	0.0007
614	2.0463	0.0047	1.536	0.0007
615	2.0461	0.0047	1.536	0.0007
616	2.046	0.0047	1.536	0.0007
617	2.0458	0.0047	1.536	0.0007
618	2.0457	0.0047	1.5359	0.0007
619	2.0456	0.0047	1.5359	0.0007
620	2.0454	0.0047	1.5359	0.0007
621	2.0453	0.0047	1.5359	0.0007
622	2.0451	0.0047	1.5359	0.0007
623	2.045	0.0047	1.5359	0.0007
624	2.0449	0.0046	1.5359	0.0007
625	2.0447	0.0046	1.5358	0.0007
626	2.0446	0.0046	1.5358	0.0007
627	2.0445	0.0046	1.5358	0.0007
628	2.0443	0.0046	1.5358	0.0007
629	2.0442	0.0046	1.5358	0.0007
630	2.0441	0.0046	1.5358	0.0007
631	2.0439	0.0046	1.5358	0.0007
632	2.0438	0.0046	1.5357	0.0007
633	2.0437	0.0046	1.5357	0.0007
634	2.0435	0.0046	1.5357	0.0007
635	2.0434	0.0045	1.5357	0.0007
636	2.0433	0.0045	1.5357	0.0007
637	2.0432	0.0045	1.5357	0.0007
638	2.043	0.0045	1.5357	0.0007
639	2.0429	0.0045	1.5357	0.0007
640	2.0428	0.0045	1.5356	0.0006
641	2.0427	0.0045	1.5356	0.0006
642	2.0425	0.0045	1.5356	0.0006
643	2.0424	0.0045	1.5356	0.0006
644	2.0423	0.0045	1.5356	0.0006
645	2.0422	0.0045	1.5356	0.0006
646	2.042	0.0044	1.5356	0.0006
647	2.0419	0.0044	1.5355	0.0006
648	2.0418	0.0044	1.5355	0.0006

649	2.0417	0.0044	1.5355	0.0006
650	2.0416	0.0044	1.5355	0.0006
651	2.0414	0.0044	1.5355	0.0006
652	2.0413	0.0044	1.5355	0.0006
653	2.0412	0.0044	1.5355	0.0006
654	2.0411	0.0044	1.5355	0.0006
655	2.041	0.0044	1.5355	0.0006
656	2.0409	0.0044	1.5354	0.0006
657	2.0407	0.0044	1.5354	0.0006
658	2.0406	0.0043	1.5354	0.0006
659	2.0405	0.0043	1.5354	0.0006
660	2.0404	0.0043	1.5354	0.0006
661	2.0403	0.0043	1.5354	0.0006
662	2.0402	0.0043	1.5354	0.0006
663	2.0401	0.0043	1.5354	0.0006
664	2.04	0.0043	1.5353	0.0006
665	2.0398	0.0043	1.5353	0.0006
666	2.0397	0.0043	1.5353	0.0006
667	2.0396	0.0043	1.5353	0.0006
668	2.0395	0.0043	1.5353	0.0006
669	2.0394	0.0043	1.5353	0.0006
670	2.0393	0.0042	1.5353	0.0006
671	2.0392	0.0042	1.5353	0.0006
672	2.0391	0.0042	1.5353	0.0006
673	2.039	0.0042	1.5352	0.0006
674	2.0389	0.0042	1.5352	0.0006
675	2.0388	0.0042	1.5352	0.0006
676	2.0387	0.0042	1.5352	0.0006
677	2.0386	0.0042	1.5352	0.0006
678	2.0385	0.0042	1.5352	0.0006
679	2.0384	0.0042	1.5352	0.0006
680	2.0383	0.0042	1.5352	0.0006
681	2.0382	0.0042	1.5352	0.0006
682	2.0381	0.0042	1.5351	0.0006
683	2.038	0.0042	1.5351	0.0006
684	2.0379	0.0041	1.5351	0.0006
685	2.0378	0.0041	1.5351	0.0006
686	2.0377	0.0041	1.5351	0.0006
687	2.0376	0.0041	1.5351	0.0006
688	2.0375	0.0041	1.5351	0.0006
689	2.0374	0.0041	1.5351	0.0006
690	2.0373	0.0041	1.5351	0.0006

691	2.0372	0.0041	1.5351	0.0006
692	2.0371	0.0041	1.535	0.0006
693	2.037	0.0041	1.535	0.0006
694	2.0369	0.0041	1.535	0.0006
695	2.0368	0.0041	1.535	0.0006
696	2.0367	0.0041	1.535	0.0006
697	2.0366	0.004	1.535	0.0006
698	2.0365	0.004	1.535	0.0006
699	2.0364	0.004	1.535	0.0006
700	2.0363	0.004	1.535	0.0006
701	2.0362	0.004	1.535	0.0006
702	2.0361	0.004	1.5349	0.0006
703	2.036	0.004	1.5349	0.0006
704	2.0359	0.004	1.5349	0.0006
705	2.0359	0.004	1.5349	0.0006
706	2.0358	0.004	1.5349	0.0006
707	2.0357	0.004	1.5349	0.0006
708	2.0356	0.004	1.5349	0.0006
709	2.0355	0.004	1.5349	0.0006
710	2.0354	0.004	1.5349	0.0006
711	2.0353	0.004	1.5349	0.0006
712	2.0352	0.0039	1.5349	0.0006
713	2.0351	0.0039	1.5348	0.0006
714	2.0351	0.0039	1.5348	0.0006
715	2.035	0.0039	1.5348	0.0006
716	2.0349	0.0039	1.5348	0.0006
717	2.0348	0.0039	1.5348	0.0006
718	2.0347	0.0039	1.5348	0.0006
719	2.0346	0.0039	1.5348	0.0006
720	2.0345	0.0039	1.5348	0.0006
721	2.0345	0.0039	1.5348	0.0005
722	2.0344	0.0039	1.5348	0.0005
723	2.0343	0.0039	1.5348	0.0005
724	2.0342	0.0039	1.5347	0.0005
725	2.0341	0.0039	1.5347	0.0005
726	2.034	0.0039	1.5347	0.0005
727	2.034	0.0038	1.5347	0.0005
728	2.0339	0.0038	1.5347	0.0005
729	2.0338	0.0038	1.5347	0.0005
730	2.0337	0.0038	1.5347	0.0005
731	2.0336	0.0038	1.5347	0.0005
732	2.0336	0.0038	1.5347	0.0005

733	2.0335	0.0038	1.5347	0.0005
734	2.0334	0.0038	1.5347	0.0005
735	2.0333	0.0038	1.5347	0.0005
736	2.0332	0.0038	1.5346	0.0005
737	2.0332	0.0038	1.5346	0.0005
738	2.0331	0.0038	1.5346	0.0005
739	2.033	0.0038	1.5346	0.0005
740	2.0329	0.0038	1.5346	0.0005
741	2.0329	0.0038	1.5346	0.0005
742	2.0328	0.0038	1.5346	0.0005
743	2.0327	0.0038	1.5346	0.0005
744	2.0326	0.0037	1.5346	0.0005
745	2.0325	0.0037	1.5346	0.0005
746	2.0325	0.0037	1.5346	0.0005
747	2.0324	0.0037	1.5346	0.0005
748	2.0323	0.0037	1.5346	0.0005
749	2.0322	0.0037	1.5345	0.0005
750	2.0322	0.0037	1.5345	0.0005
751	2.0321	0.0037	1.5345	0.0005
752	2.032	0.0037	1.5345	0.0005
753	2.032	0.0037	1.5345	0.0005
754	2.0319	0.0037	1.5345	0.0005
755	2.0318	0.0037	1.5345	0.0005
756	2.0317	0.0037	1.5345	0.0005
757	2.0317	0.0037	1.5345	0.0005
758	2.0316	0.0037	1.5345	0.0005
759	2.0315	0.0037	1.5345	0.0005
760	2.0315	0.0037	1.5345	0.0005
761	2.0314	0.0036	1.5345	0.0005
762	2.0313	0.0036	1.5344	0.0005
763	2.0312	0.0036	1.5344	0.0005
764	2.0312	0.0036	1.5344	0.0005
765	2.0311	0.0036	1.5344	0.0005
766	2.031	0.0036	1.5344	0.0005
767	2.031	0.0036	1.5344	0.0005
768	2.0309	0.0036	1.5344	0.0005
769	2.0308	0.0036	1.5344	0.0005
770	2.0308	0.0036	1.5344	0.0005
771	2.0307	0.0036	1.5344	0.0005
772	2.0306	0.0036	1.5344	0.0005
773	2.0306	0.0036	1.5344	0.0005
774	2.0305	0.0036	1.5344	0.0005

775	2.0304	0.0036	1.5344	0.0005
776	2.0304	0.0036	1.5344	0.0005
777	2.0303	0.0036	1.5343	0.0005
778	2.0302	0.0036	1.5343	0.0005
779	2.0302	0.0035	1.5343	0.0005
780	2.0301	0.0035	1.5343	0.0005
781	2.03	0.0035	1.5343	0.0005
782	2.03	0.0035	1.5343	0.0005
783	2.0299	0.0035	1.5343	0.0005
784	2.0298	0.0035	1.5343	0.0005
785	2.0298	0.0035	1.5343	0.0005
786	2.0297	0.0035	1.5343	0.0005
787	2.0296	0.0035	1.5343	0.0005
788	2.0296	0.0035	1.5343	0.0005
789	2.0295	0.0035	1.5343	0.0005
790	2.0295	0.0035	1.5343	0.0005
791	2.0294	0.0035	1.5343	0.0005
792	2.0293	0.0035	1.5342	0.0005
793	2.0293	0.0035	1.5342	0.0005
794	2.0292	0.0035	1.5342	0.0005
795	2.0291	0.0035	1.5342	0.0005
796	2.0291	0.0035	1.5342	0.0005
797	2.029	0.0035	1.5342	0.0005
798	2.029	0.0035	1.5342	0.0005
799	2.0289	0.0034	1.5342	0.0005
800	2.0288	0.0034	1.5342	0.0005
801	2.0288	0.0034	1.5342	0.0005
802	2.0287	0.0034	1.5342	0.0005
803	2.0287	0.0034	1.5342	0.0005
804	2.0286	0.0034	1.5342	0.0005
805	2.0285	0.0034	1.5342	0.0005
806	2.0285	0.0034	1.5342	0.0005
807	2.0284	0.0034	1.5342	0.0005
808	2.0284	0.0034	1.5341	0.0005
809	2.0283	0.0034	1.5341	0.0005
810	2.0283	0.0034	1.5341	0.0005
811	2.0282	0.0034	1.5341	0.0005
812	2.0281	0.0034	1.5341	0.0005
813	2.0281	0.0034	1.5341	0.0005
814	2.028	0.0034	1.5341	0.0005
815	2.028	0.0034	1.5341	0.0005
816	2.0279	0.0034	1.5341	0.0005

817	2.0279	0.0034	1.5341	0.0005
818	2.0278	0.0034	1.5341	0.0005
819	2.0277	0.0033	1.5341	0.0005
820	2.0277	0.0033	1.5341	0.0005
821	2.0276	0.0033	1.5341	0.0005
822	2.0276	0.0033	1.5341	0.0005
823	2.0275	0.0033	1.5341	0.0005
824	2.0275	0.0033	1.5341	0.0005
825	2.0274	0.0033	1.534	0.0005
826	2.0274	0.0033	1.534	0.0005
827	2.0273	0.0033	1.534	0.0005
828	2.0273	0.0033	1.534	0.0005
829	2.0272	0.0033	1.534	0.0005
830	2.0271	0.0033	1.534	0.0005
831	2.0271	0.0033	1.534	0.0005
832	2.027	0.0033	1.534	0.0005
833	2.027	0.0033	1.534	0.0005
834	2.0269	0.0033	1.534	0.0005
835	2.0269	0.0033	1.534	0.0005
836	2.0268	0.0033	1.534	0.0005
837	2.0268	0.0033	1.534	0.0005
838	2.0267	0.0033	1.534	0.0005
839	2.0267	0.0033	1.534	0.0005
840	2.0266	0.0033	1.534	0.0005
841	2.0266	0.0032	1.534	0.0004
842	2.0265	0.0032	1.534	0.0004
843	2.0265	0.0032	1.534	0.0004
844	2.0264	0.0032	1.5339	0.0004
845	2.0264	0.0032	1.5339	0.0004
846	2.0263	0.0032	1.5339	0.0004
847	2.0263	0.0032	1.5339	0.0004
848	2.0262	0.0032	1.5339	0.0004
849	2.0262	0.0032	1.5339	0.0004
850	2.0261	0.0032	1.5339	0.0004
851	2.0261	0.0032	1.5339	0.0004
852	2.026	0.0032	1.5339	0.0004
853	2.026	0.0032	1.5339	0.0004
854	2.0259	0.0032	1.5339	0.0004
855	2.0259	0.0032	1.5339	0.0004
856	2.0258	0.0032	1.5339	0.0004
857	2.0258	0.0032	1.5339	0.0004
858	2.0257	0.0032	1.5339	0.0004

859	2.0257	0.0032	1.5339	0.0004
860	2.0256	0.0032	1.5339	0.0004
861	2.0256	0.0032	1.5339	0.0004
862	2.0255	0.0032	1.5339	0.0004
863	2.0255	0.0032	1.5339	0.0004
864	2.0254	0.0032	1.5338	0.0004
865	2.0254	0.0031	1.5338	0.0004
866	2.0254	0.0031	1.5338	0.0004
867	2.0253	0.0031	1.5338	0.0004
868	2.0253	0.0031	1.5338	0.0004
869	2.0252	0.0031	1.5338	0.0004
870	2.0252	0.0031	1.5338	0.0004
871	2.0251	0.0031	1.5338	0.0004
872	2.0251	0.0031	1.5338	0.0004
873	2.025	0.0031	1.5338	0.0004
874	2.025	0.0031	1.5338	0.0004
875	2.0249	0.0031	1.5338	0.0004
876	2.0249	0.0031	1.5338	0.0004
877	2.0249	0.0031	1.5338	0.0004
878	2.0248	0.0031	1.5338	0.0004
879	2.0248	0.0031	1.5338	0.0004
880	2.0247	0.0031	1.5338	0.0004
881	2.0247	0.0031	1.5338	0.0004
882	2.0246	0.0031	1.5338	0.0004
883	2.0246	0.0031	1.5338	0.0004
884	2.0245	0.0031	1.5338	0.0004
885	2.0245	0.0031	1.5337	0.0004
886	2.0245	0.0031	1.5337	0.0004
887	2.0244	0.0031	1.5337	0.0004
888	2.0244	0.0031	1.5337	0.0004
889	2.0243	0.0031	1.5337	0.0004
890	2.0243	0.003	1.5337	0.0004
891	2.0242	0.003	1.5337	0.0004
892	2.0242	0.003	1.5337	0.0004
893	2.0242	0.003	1.5337	0.0004
894	2.0241	0.003	1.5337	0.0004
895	2.0241	0.003	1.5337	0.0004
896	2.024	0.003	1.5337	0.0004
897	2.024	0.003	1.5337	0.0004
898	2.0239	0.003	1.5337	0.0004
899	2.0239	0.003	1.5337	0.0004
900	2.0239	0.003	1.5337	0.0004

901	2.0238	0.003	1.5337	0.0004
902	2.0238	0.003	1.5337	0.0004
903	2.0237	0.003	1.5337	0.0004
904	2.0237	0.003	1.5337	0.0004
905	2.0237	0.003	1.5337	0.0004
906	2.0236	0.003	1.5337	0.0004
907	2.0236	0.003	1.5337	0.0004
908	2.0235	0.003	1.5337	0.0004
909	2.0235	0.003	1.5336	0.0004
910	2.0235	0.003	1.5336	0.0004
911	2.0234	0.003	1.5336	0.0004
912	2.0234	0.003	1.5336	0.0004
913	2.0233	0.003	1.5336	0.0004
914	2.0233	0.003	1.5336	0.0004
915	2.0233	0.003	1.5336	0.0004
916	2.0232	0.0029	1.5336	0.0004
917	2.0232	0.0029	1.5336	0.0004
918	2.0231	0.0029	1.5336	0.0004
919	2.0231	0.0029	1.5336	0.0004
920	2.0231	0.0029	1.5336	0.0004
921	2.023	0.0029	1.5336	0.0004
922	2.023	0.0029	1.5336	0.0004
923	2.023	0.0029	1.5336	0.0004
924	2.0229	0.0029	1.5336	0.0004
925	2.0229	0.0029	1.5336	0.0004
926	2.0228	0.0029	1.5336	0.0004
927	2.0228	0.0029	1.5336	0.0004
928	2.0228	0.0029	1.5336	0.0004
929	2.0227	0.0029	1.5336	0.0004
930	2.0227	0.0029	1.5336	0.0004
931	2.0227	0.0029	1.5336	0.0004
932	2.0226	0.0029	1.5336	0.0004
933	2.0226	0.0029	1.5336	0.0004
934	2.0225	0.0029	1.5335	0.0004
935	2.0225	0.0029	1.5335	0.0004
936	2.0225	0.0029	1.5335	0.0004
937	2.0224	0.0029	1.5335	0.0004
938	2.0224	0.0029	1.5335	0.0004
939	2.0224	0.0029	1.5335	0.0004
940	2.0223	0.0029	1.5335	0.0004
941	2.0223	0.0029	1.5335	0.0004
942	2.0223	0.0029	1.5335	0.0004

943	2.0222	0.0029	1.5335	0.0004
944	2.0222	0.0029	1.5335	0.0004
945	2.0222	0.0028	1.5335	0.0004
946	2.0221	0.0028	1.5335	0.0004
947	2.0221	0.0028	1.5335	0.0004
948	2.022	0.0028	1.5335	0.0004
949	2.022	0.0028	1.5335	0.0004
950	2.022	0.0028	1.5335	0.0004
951	2.0219	0.0028	1.5335	0.0004
952	2.0219	0.0028	1.5335	0.0004
953	2.0219	0.0028	1.5335	0.0004
954	2.0218	0.0028	1.5335	0.0004
955	2.0218	0.0028	1.5335	0.0004
956	2.0218	0.0028	1.5335	0.0004
957	2.0217	0.0028	1.5335	0.0004
958	2.0217	0.0028	1.5335	0.0004
959	2.0217	0.0028	1.5335	0.0004
960	2.0216	0.0028	1.5335	0.0004
961	2.0216	0.0028	1.5335	0.0004
962	2.0216	0.0028	1.5334	0.0004
963	2.0215	0.0028	1.5334	0.0004
964	2.0215	0.0028	1.5334	0.0004
965	2.0215	0.0028	1.5334	0.0004
966	2.0214	0.0028	1.5334	0.0004
967	2.0214	0.0028	1.5334	0.0004
968	2.0214	0.0028	1.5334	0.0004
969	2.0213	0.0028	1.5334	0.0004
970	2.0213	0.0028	1.5334	0.0004
971	2.0213	0.0028	1.5334	0.0004
972	2.0212	0.0028	1.5334	0.0004
973	2.0212	0.0028	1.5334	0.0004
974	2.0212	0.0028	1.5334	0.0004
975	2.0211	0.0028	1.5334	0.0004
976	2.0211	0.0027	1.5334	0.0004
977	2.0211	0.0027	1.5334	0.0004
978	2.021	0.0027	1.5334	0.0004
979	2.021	0.0027	1.5334	0.0004
980	2.021	0.0027	1.5334	0.0004
981	2.021	0.0027	1.5334	0.0004
982	2.0209	0.0027	1.5334	0.0004
983	2.0209	0.0027	1.5334	0.0004
984	2.0209	0.0027	1.5334	0.0004

985	2.0208	0.0027	1.5334	0.0004
986	2.0208	0.0027	1.5334	0.0004
987	2.0208	0.0027	1.5334	0.0004
988	2.0207	0.0027	1.5334	0.0004
989	2.0207	0.0027	1.5334	0.0004
990	2.0207	0.0027	1.5334	0.0004
991	2.0206	0.0027	1.5334	0.0004
992	2.0206	0.0027	1.5334	0.0004
993	2.0206	0.0027	1.5333	0.0004
994	2.0206	0.0027	1.5333	0.0004
995	2.0205	0.0027	1.5333	0.0004
996	2.0205	0.0027	1.5333	0.0004
997	2.0205	0.0027	1.5333	0.0004
998	2.0204	0.0027	1.5333	0.0004
999	2.0204	0.0027	1.5333	0.0004
1000	2.0204	0.0027	1.5333	0.0004

References

- 1 Fujiwara, H. *Spectroscopic ellipsometry: principles and applications*. (John Wiley & Sons, 2007).
- 2 Arnaud, B., Lebègue, S., Rabiller, P. & Alouani, M. Huge excitonic effects in layered hexagonal boron nitride. *Physical review letters* **96**, 026402 (2006).
- 3 Artús, L. *et al.* Ellipsometry study of hexagonal boron nitride using synchrotron radiation: transparency window in the Far-UV. *Advanced Photonics Research* **2**, 2000101 (2021).
- 4 Tarrío, C. & Schnatterly, S. Interband transitions, plasmons, and dispersion in hexagonal boron nitride. *Physical review B* **40**, 7852 (1989).
- 5 Pettersson, L. A., Roman, L. S. & Inganäs, O. Modeling photocurrent action spectra of photovoltaic devices based on organic thin films. *Journal of Applied Physics* **86**, 487-496 (1999).
- 6 Peumans, P., Yakimov, A. & Forrest, S. R. Small molecular weight organic thin-film photodetectors and solar cells. *Journal of Applied Physics* **93**, 3693-3723 (2003).
- 7 Passler, N. C. & Paarmann, A. Generalized 4× 4 matrix formalism for light propagation in anisotropic stratified media: study of surface phonon polaritons in polar dielectric heterostructures. *Journal of the Optical Society of America B* **34**, 2128-2139 (2017).
- 8 Choi, B. *et al.* Giant Optical Anisotropy in 2D Metal–Organic Chalcogenates. *ACS Nano* **18**, 25489-25498 (2024). <https://doi.org/10.1021/acsnano.4c05043>
- 9 Ermolaev, G. *et al.* Giant optical anisotropy in transition metal dichalcogenides for next-generation photonics. *Nature communications* **12**, 854 (2021).
- 10 Wemple, S. H., Didomenico, M. & Camlibel, I. Dielectric and optical properties of melt-grown BaTiO₃. *Journal of Physics and Chemistry of Solids* **29**, 1797-1803 (1968). [https://doi.org/https://doi.org/10.1016/0022-3697\(68\)90164-9](https://doi.org/https://doi.org/10.1016/0022-3697(68)90164-9)
- 11 Ghosh, G. Dispersion-equation coefficients for the refractive index and birefringence of calcite and quartz crystals. *Optics communications* **163**, 95-102 (1999).
- 12 Yang, H. *et al.* Optical Waveplates Based on Birefringence of Anisotropic Two-Dimensional Layered Materials. *ACS Photonics* **4**, 3023-3030 (2017). <https://doi.org/10.1021/acsp Photonics.7b00507>
- 13 Munkhbat, B., Wróbel, P., Antosiewicz, T. J. & Shegai, T. O. Optical Constants of Several Multilayer Transition Metal Dichalcogenides Measured by Spectroscopic Ellipsometry in the 300–1700 nm Range: High Index, Anisotropy, and Hyperbolicity. *ACS Photonics* **9**, 2398-2407 (2022). <https://doi.org/10.1021/acsp Photonics.2c00433>
- 14 Niu, S. *et al.* Giant optical anisotropy in a quasi-one-dimensional crystal. *Nature Photonics* **12**, 392-396 (2018).
- 15 Guo, Q. *et al.* Colossal in-plane optical anisotropy in a two-dimensional van der Waals crystal. *Nature Photonics*, 1-6 (2024).
- 16 Zhang, H. *et al.* Cavity-enhanced linear dichroism in a van der Waals antiferromagnet. *Nature Photonics* **16**, 311-317 (2022).
- 17 Novotny, L. & Hecht, B. *Principles of nano-optics*. (Cambridge university press, 2012).
- 18 Chebykin, A., Orlov, A., Shalin, A., Poddubny, A. & Belov, P. Strong Purcell effect in anisotropic ϵ -near-zero metamaterials. *Physical Review B* **91**, 205126 (2015).
- 19 Bharadwaj, P. & Novotny, L. Spectral dependence of single molecule fluorescence enhancement. *Optics express* **15**, 14266-14274 (2007).
- 20 Maier, S. A. *Plasmonics: fundamentals and applications*. Vol. 1 (Springer, 2007).
- 21 Jackson, E., Tischler, J., Ratchford, D. & Ellis, C. The role of losses in determining hyperbolic material figures of merit. *Scientific Reports* **14**, 25156 (2024).

